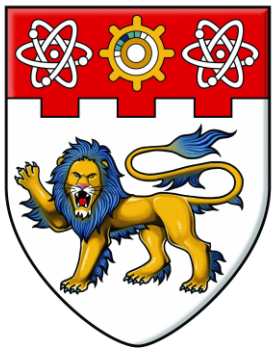

NANYANG TECHNOLOGICAL UNIVERSITY

OXYGEN K-EDGE X-RAY ABSORPTION SPECTROSCOPY STUDY IN ICE AND MOLECULAR DYANMICS STUDY IN HYDROGEN HYDRATE: DENSITY FUNTIONAL THEORY APPLICAITONS

ZHANG JINGYUN

DIVISION OF PHYSICS & APPLIED PHYSICS

SCHOOL OF PHYSICAL & MATHEMATICAL SCIENCES

NANYANG THECHNOLOGICAL UNIVERSITY

2012

OXYGEN K-EDGE X-RAY ABSORPTION SPECTROSCOPY STUDY IN ICE AN
MOLECULAR DYANMICS STUDY IN HYDROGEN HYDRATE
ZHANG JINGYUN
2012

OXYGEN K-EDGE X-RAY ABSORPTION SPECTROSCOPY STUDY IN ICE AND MOLECULAR DYANMICS STUDY IN HYDROGEN HYDRATE: DENSITY FUNTIONAL THEORY APPLICAITONS

ZHANG JINGYUN

SCHOOL OF PHYSICAL AND MATHEMATICAL SCIENCES

A thesis submitted to the Nanyang Technological University

In fulfillment of the requirement for the degree of

Doctor of Philosophy

2012

ACKNOWLEDGMENTS

There have been many people involved in my Ph. D study. Here follows an uncomplete list of people that in one way or another are appreciated for their help, support, and friendship.

First of all, I would like to express my sincere gratitude and dedicated appreciation to my supervisors Prof. Shen Zexiang, Dr. Kuo Jer-Lai, and Dr. Toshiaki IITAKA. I could not finish my Ph. D research project without their invaluable assistances, supports, and patient guidance.

Furthermore, special thanks were addressed to the people that I worked with. In particular, Dr. Fan Xiaofeng gave me many inspiring ideas and Dr. Nguyen Quoc Chinh helped me a lot on the programming. Also, nice atmosphere in the lab would not form without Dr. Bing Dan, Mr. Wu Hongyu for sharing the literatures and life experiences together.

Last but not least, I would like to thank my beloved parents for their always love and encouragement during my study and my daily life. Their steady supports motivate me a lot when I came across difficulties. This work was dedicated to my father and my mother.

Financial support from Nanyang Technological University is acknowledged.

Table of contents

Chapter 6 Conclusions and future work

Summary

Many properties of the water in the physics concern are not well understood. In particular, there is still no consensus on the water structure even at the presence of the conventional tetrahedral model. In this thesis, we proposed that oxygen *K* edge X-ray absorption spectroscopy (XAS) might be an effective tool to extract the local structure information in water system. On the other hand, the ice-relating material hydrogen hydrate was found to have a pressure-induce phase transition around 40 GPa while the new structure remains unsolved. With the aim to shed some light on the structure of the new phase structure, we carried out first principle molecular dynamic study on hydrogen hydrate under pressure.

It is well known that structure is the very first step for properties investigation. In ice, each water molecule connected to four other water molecules obeying the ice rule. The number of possible configurations for the N molecules unit cell grows exponentially as $(3/2)^N$. We could enumerate all the possible hydrogen bond configurations with the help of graph theory and then refine the structures with density function theory (DFT) to locate the most stable configuration. Taking ice XIII as an example which is the most complicated ice phase out of its 15 known phases, we demonstrated that DFT could successfully predict the ground state structure which gives us further confidence in the following studies on the oxygen *K* edge XAS in ice system.

Oxygen *K* edge XAS is believed to be an effective structural tool relying on the fact that it could probe the local instantaneous environments around the excited atom. In ice I_h, our calculations achieved a good agreement with experimental spectrum of oxygen *K* edge XAS in spectral features (spectral peaks and relative intensity). Stepwise inclusion of different types of interactions (half core hole and full core hole model) within DFT, together with a supercell model, showed that core hole effects must be included in order to describe the changes in electronic structure as reflected in experimental oxygen *K* edge XAS. We found that the pre-edge feature (~535 eV) is a universal signal in different crystalline phases except ice X. Moreover, main peak region (~ 537-540 eV) shows sensitivity to the local hydrogen bond network.

Through the analyzing of the projected electronic density of states, we identified the origin of the oxygen *K* edge XAS spectral features in which transitions of oxygen 1*s*-4a_1 contribute mainly to the pre-edge while the oxygen 1*s*-2b_2 transitions give rise to the main peak feature. The disappearance of pre-edge in ice X can be interpreted as the symmetrization of hydrogen bond which makes the 4a_1 orbitals pure *s*-character. The sensitivity to the local hydrogen bond configuration, in particular the sensitivity to broken bonds on the donor side is due to the fact that water is a highly polarized molecule. As we all know, oxygen atoms possessed higher electronegativity than hydrogen atoms, hence, the polarization points from hydrogen atom to oxygen atoms in the occupied states. Concerning the orbital orthogonality, the polarization is towards hydrogen atoms of the unoccupied states which makes the XAS is more sensitive to the local environment around the hydrogen side. From this, we could connect the linkage between pre-edge and the broken hydrogen bond and this is

expected to shed some light on the recent controversy on the pre-edge explanation which can be referred in more details as discussed in Chap. 4.

The second section of this thesis is focusing on the structural and vibrational properties study of filled ice C_2 hydrogen hydrate under compression by first principles molecular dynamics (FPMD). The filled ice hydrate C_2 is composed by a host ice I_c structure while the hydrogen molecules located in the interstitials of ice I_c structure while the molecular ratio of hydrogen to water is 1:1. In particular, phase transitions under pressure have been investigated using x-ray diffraction (XRD) and Raman spectroscopy. In the low pressure region, C_2 hydrogen hydrate remains a cubic crystal structure and the structural transitions were observed at approximately 35-40 and 55-60 GPa and the high-pressure phase can survive up to at least 80.3 GPa. However, these two high-pressure phases have not been refined by the experimentalists.

It is essential to note that the experimentally reported cubic Fd-3m (space group) C_2 phase reflects the symmetry at high (room) temperature when the hydrogen bond network is disordered and the hydrogen molecules are orientationally disordered. In this sense, the "*cubic*" symmetry would definitely be lowered at low temperature where the hydrogen bond network is ordered and the hydrogen molecules are aligned. Indeed, we found tetragonal symmetry ($P4_12_12$ and $Pna2_1$ space group) in our FPMD at low temperature. This finding demonstrates that the thermal effects play an essential role in stabilizing the structure to appear as cubic below 40 GPa. We also observed an indication of transition to an unknown high pressure phase above 40 GPa which is consistent with the experimental findings. Moreover, we determined the phase

boundary line between hydrogen bond ordered (disordered) phases and the H_2 rotation and non-rotation phases at a rough approximation which may provide hints for further experiments. The vibrational frequencies are extracted from Fourier analysis of the MD trajectories, which are in good agreement with experimental data in the frequency peak positions. Hydrogen bond is predicted to symmetrize below 60 GPa based on the analysis of O-H stretching frequencies and radial distribution function g(OH). In comparison with the pure ice VII, the hydrogen bond symmetrization pressure in C_2 hydrogen hydrate is much lower, being reduced by a factor of two.

List of Figures

List of Table

Abbreviations

DFT	Density functional theory
LDA	Local density approximation
GGA	Generalized gradient approximation
H-bond	Hydrogen bond
XAS	X-ray absorption spectroscopy
XRD	X-ray diffraction
MD	Molecular dynamics
RDF	Radial distribution function

Publications

Journal publications related to the thesis

1. ***Jingyun Zhang***, Zhi-Ren Xiao, and Jer-Lai Kuo, "*Calculation of near K edge x-ray absorption spectra and hydrogen bond network in ice XIII under compression*" J. Chem. Phys., **132,** 184506 (2010)
2. Xiaofeng Fan, Dan Bing, ***Jingyun Zhang***, Zexiang Shen, and Jer-Lai Kuo, "*Predicting the hydrogen bond ordered structures of ice Ih, II, III, VI and ice VII: DFT methods with localized based set"*, Comp. Mater. Sci. **49**, S170 (2010)
3. Jingyun Zhang, Jer-Lai Kuo, and Toshiaki Iitaka, "First principles moleculear dynamics study of filled ice hydrogen hydrate", J. Chem. Phys., **137,** 084505 (2012)

Conference publications related to the thesis

1. ***Jingyun Zhang*** and Jer-lai Kuo, "*First principles molecular dynamics study on filled ice hydrogen hydrate under pressure*" Sep.5-10, 2010, 12th International Conference on the Physics and Chemistry of Ice, Sapporo, Japan.
2. ***Jingyun Zhang***, Jer-Lai Kuo, Toshiaki Iitaka "*First principles molecular dynamics study on filled ice hydrogen hydrate under pressure*", Nov. 7-12, 2010, 5th Asian Conference on High Pressure Research, Japan.
3. ***Jingyun Zhang*** and Jer-lai Kuo, "*Oxygen K edge X-ray absorption spectra and hydrogen bond network in ice XIII under compression: an ab initio calculation*" Jan. 10-11, 2010, The 4th Cross-Strait Theoretical and Computational Chemistry Conference, Kinmen, Taiwan.

Journal publications related to other projects

1. ***Jingyun Zhang*** and Jer-Lai Kuo, " *Phonon and elastic instabilities in rocksalt calcium oxide under pressure: A first-principles study*", J. Phys. Cond. Matt. **21**, 015402 (2009)
2. Yan Yan, ***Jingyun Zhang*** , Tian Cui, Yan Li, Yanming Ma,J.Gong ,Z.G.Zong, Guangtian Zou, "*First-principles study of high pressure phase transformations in Li3N*" Eur. Phys. J. B, **61**, 397 (2008)
3. ***Jingyun Zhang***, Lijun Zhang, Tian Cui,,Yingli Niu, Zhi He, Yanming Ma,Guangtian Zou, "*A first-principles study of electron–phonon coupling in electron-doped LiH*" *J. Phys. Cond. Matt.* **19**, 425218 (2007)
4. ***Jingyun Zhang***, Lijun Zhang, Tian Cui, Yan Li, Zhi He, Yanming Ma,Guangtian Zou, "*Phonon and Elastic instabilities in Rocksalt Alkali Hydrides under Pressure: A First-principles Study*" Physical Review B **75**, 104115 (2007)

Conference publications related to other projects

1. ***Jingyun Zhang*** and Jer-lai Kuo, "*Phonon and Elastic instabilities in Rocksalt Calcium Oxide under Pressure: A First-principles Study*", 3rd MRS-S Conference on Advanced Materials, Feb. 25 – 27, 2008, Singapore.

Chapter 1

Introduction

1.1 An overview of ice

1.1.1 Phase diagram of water

Water is the most abundant compound on the Earth's surface and the principal constituent of all living organisms which acts a crucial role in numerous biological, physical and chemical processes.[1] In particular, the water substance exhibits a fascinating range of solid phases more than any other known material, and all of these phases are referred to as forms of "ice". Ice I_h exsits stably at ambient conditions and the number of its various phases is up to at least sixteen[2] established so far. Most of these phases are synthesized under the application of pressure, which result in denser packing of molecules than in ice I_h. And water is denser than ice I_h, this is the reason that ordinary ice can float on the water surface. All in all, the peculiar properties of water and its complex phase diagram could be attributed to the versatility of the hydrogen bond interaction.

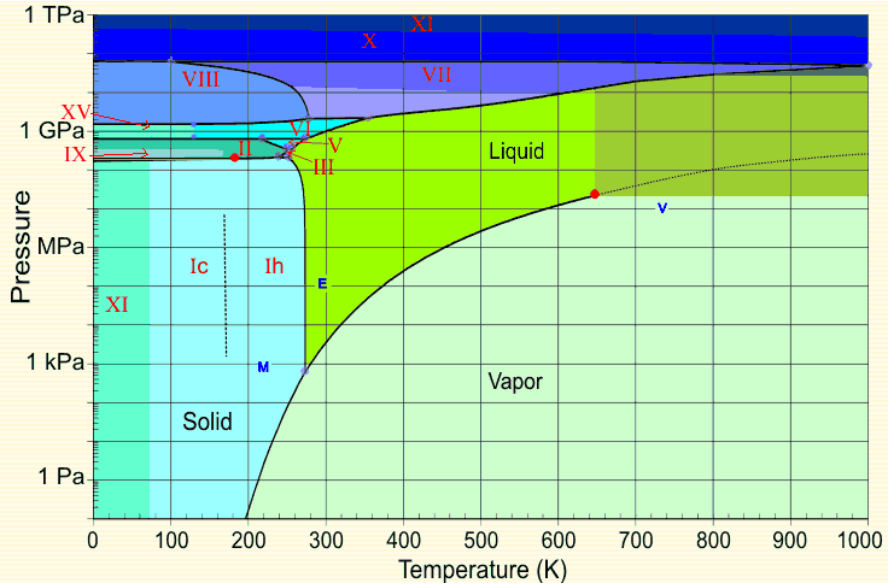

Fig. 1.1 Phase diagram of water (http://www.lsbu.ac.uk/water/phase.html)

1.1.2 Hydrogen bond

Many properties of water remain elusive until now in which the structure, bonding and dynamics of water in many different chemical situations is poorly understood. The problem could be understood as to the nature of the hydrogen bond whose strength (~5 kcal/mole) intermediates between these strong covalent bonds (~100 kcal/mole) and weak van der Waals forces (~0.3 kcal/mole)[3,4]. This makes it strong enough to create stable structures but also weak enough to be broken at ambient temperature. Hence, this creates puzzles and fascinating properties in different hydrogen bond situation and processes. This in itself shows that there are fundamental aspects of the forces involved in the hydrogen bond that are disregarded or poorly described.

Hydrogen bond, a molecular interaction was discovered in the early 1920s[5] and promptly recognized to play a very important role in many chemical and biological

phenomena. In water system, hydrogen bonding is the tendency of water molecules to arrange so that the OH bond of one water (the donor) points directly (see Figure 1.2). Due to its specific properties and immense importance in nature, hydrogen bond is classified as a separate type of chemical interaction.

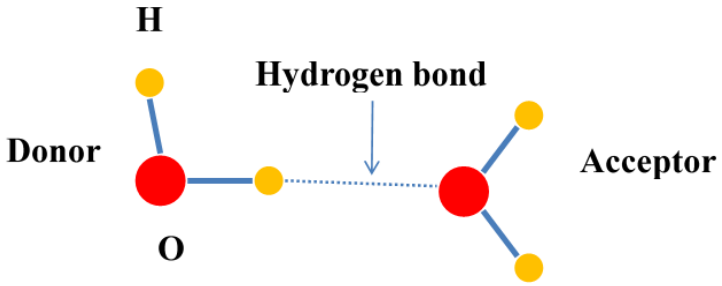

Fig. 1.2 Schematic picture of hydrogen bond in which the oxygen and hydrogen atoms are represented as red and yellow balls, respectively; OH covalent bond and hydrogen bond are represented by the solid blue lines and dotted blue line, respectively.

There are several ways to describe hydrogen bond in a quantitative way. One common way is to restrict the two neighboring oxygen atoms' distance smaller than 3.5 Å and the H-O ··O angle smaller than 30^{o}[6]. Another way is calculating the binding energies distribution of the water molecule pairs and the first peak is assigned as the hydrogen bond[3]. There are reports using study the hydrogen bond in terms of electronic structure[7].

1.1.3 Disorder-order transitions

The unusual residual entropy of ice I_h has attracted a lot attention from both physicists and chemists including three Nobel laureates Giauque, Pauling and Onsager.

Giauque and his co-workers carried out a series of classical thermodynamic measurements in the 1930s[8,9] and found this non-zero entropy. In 1935, Pauling[10] calculated the residual entropy by proposing there are $(3/2)^N$ possible arrangements to put *N* water molecules in ice I_h lattice based on the four-vertex model. In the following year, measurements of the entropy in ice I_h at extremely low temperature (~ 0 K) was observed to be $Nk_B\ln(3/2)$ within experimental error.[9] It is so amazing that he arrived at the remarkably agreement through pure theoretical derivation with the experimental measurements of Giauque and Stout being $(1.5069)^N$. Since then, discussions and debate on whether there exists a completely proton-ordered counterpart of ice I_h and also arguments on this proton ordered phase ice XI to be ferroelectric or antiferroelectric have lasted for a very long period. More recently, "spin ice" materials whose magnetic moments follows similar ice rule constraint and exhibit a similar $Nk_B\ln(3/2)$ residual entropy.[11] Therefore, probing the hydrogen bond network in ice also may also provide helpful indications for understanding the "spin ice" materials.

In 1982, Suga's group demonstrated that a phase transition in ice I_h doped with KOH and it slightly depends on the dopant concentration[12]. This proton-ordering transition could be understood as the hydroxide ion catalyze hydrogen bond rearrangements and enable it approach to the equilibrium state. The nature of the ice I_h to ice XI phase transition has raised a lot of debates concerning about the ice XI to be ferroelectric or antiferroelectric[13-15]. Upon cooling in the proton disordered ice III, Whalley *et al.* reported that the transformation from ice III to an anti-ferroelectric phase, named ice IX[16] at 164.5 K. This was further confirmed by the neutron diffraction measurements.[17] Proton ordering in ice VII/VIII initiated around 2.1 GPa

which was clearly observed.[18,19] Such disorder-order transitions might be extremely slow and these processes are kinetically forbidden. In 2006, ice XIII and XIV were successfully synthesized by Salzmann *et al*[20]. In the pressure range 0.5-1.2 GPa, HCl doped hydrogen disordered ice V and ice XII were cooled to 77 K to facilitate the proton ordering process. Structural information was obtained by neutron diffraction in the unloading manner. The authors[20] claimed that "It would be a challenging test of the ability of modern day computational methods to reproduce our experimentally found lowest energy state. This would provide a critical test for current water potentials widely used in computational chemistry and structural biology." This also composes a strong motivation of our work to capture the ground state structure of ice XIII from the theoretical point of view with the aim to show the DFT robustness in the study in ice system.

1.1.4 Theoretical study in ice

One of the theoretical challenges in study ice is that the huge pool for all the possible hydrogen bond topologies allowed in a lattice of N water molecules grows roughly as $(3/2)^N$.[10] In crystalline ice, each water molecule is fully coordinated to other four molecules in a near tetrahedral symmetry through hydrogen bonds. Within the so-called Bernal-Fowler "ice-rules"[21], it is free to place two internal hydrogen bonds in any of the four given directions. Many more sophisticated empirical potentials have been designed to better fit experimental data and/or *ab* initio calculations. These empirical potential might work very well under the conditions they were parameterized, however, their transferability is limited. In particular, the SPC/E[22]

model potential was found unsuitable for the calculation phase diagram of ice which predicted that ice I_h was stable only at negative pressure; TIP4P[23] could not show the negative Clapeyron sloped observed in experiment for in VII/VIII transition and failed to predict the lowest energy structure of the hydrogen-ordered form of ice I_h, i.e. XI, indeed, no model potential has predicted the C*mc*2_1 structure to have the lowest energy.[15,24] On the other hand, *ab* initio molecular simulation methods has been developed with exciting advances in the past decade[25] and has achieved much success. Recently, first principles methods in conjunction with a theoretical tool, named graph invariants, have demonstrated their capabilities in reproducing the detailed structure information in ice systems.[26-29] Determining the ground state of different ice phases, the lowest energy hydrogen bonding arrangements is not a trivial task since the number of the possible topologies grows exponentially with system size. In this thesis, this challenge from the experimentalist (see section 1.1.3) is taken and we have demonstrated that density functional theory (DFT) methods have successfully reproduced the experimentally found structure as illustrated in Chap. 3.

1.2 Clathrate hydrate

The clathrate hydrates are ice-like crystalline materials which consist of 'host' hydrogen bonded water molecules within which are incorporated a small number of 'guest' molecules, like O_2, N_2, CH_4, H_2, CO_2 etc. Methane hydrates are considered to be a potential energy resource since enormous reserves can be found under continental shelves and permafrost. Recently, hydrogen hydrate (H_2-H_2O) receives active attention since its properties have useful implications in planetary research and it is

environment-friendly. When consuming the H_2-H_2O, the only by-product is H_2O, hence, no global warming effects. So far, there are three phases observed in experiments. One is the clathrate hydrate SII structure[30-33], the other two are filled ice structures, C_1 and C_2.[34,35] The molecular ratios of H_2:H_2O of filled ice structures, C_1 and C_2 are 1:6 and 1:1, respectively. This high hydrogen storage capacity makes it possible that the hydrogen hydrate works as a potential medium for reserving hydrogen.

1.3 X-ray absorption spectroscopy (XAS)

1.3.1 Basic physics picture of XAS

Rapid advancements in the experimental techniques in spectroscopy are of great importance to our understanding of materials and offer a way to study the materials at the molecular level. XAS is a unique tool for studying the local structure around selected elements at the atomic and molecular scale. XAS can be applied not only to crystal, but also materials that possess little or no long range translational order: amorphous systems, glasses, qusicrystals, disordered films, membranes, solutions, liquids, metalloproteins, and even molecular gases.

Intrinsically, XAS arises from the X-ray photoelectric effects in which an incident X-ray photon kicks out an electron from an inner atomic orbital of the atom within the sample. The photoelectron wave scatters from the atoms around the absorbing atom, creating interferences between outgoing and scattered parts of the photoelectron wavefunction. The X-ray absorption probability varies with the incident photon energy and this is proportional to the X-ray absorption coefficient $\mu(E)$, a

basic physical quantity that is measured in XAS. Generally, $\mu(E)$ smoothly decreases as the energy increases (approximately $1/E^3$), i.e. the X-rays become more penetrating. However, there are sudden increases of absorption coefficient at some certain photon energy (elemental specific) which was called X-ray absorption edges.

Near Edge X-Ray Absorption Fine Structure Spectroscopy (NEXAFS) is referred to the first 30 eV which was featured by greatest changes in the absorption coefficient and intense, narrow resonances. Often, X-ray Absorption Near Edge Structure (XANES) is also referred as NEXAFS. However, conventionally, NEXAFS is used for soft X-ray spectroscopy while XANES is usually for hard X-ray spectra. For the extended X-ray absorption fine structure (EXAFS), the energy range to be investigated is beyond 30 eV while the XANES examined the first 30 eV above the edge.

NEXAFS shows great sensitivity to the surrounding environment of the absorbing atom and multiple scattering theory applies here. The excited electron is scattered by its neighboring atoms and this photoelectron was used as a probe for the local bonding networks. Secondly, the excitation time for the core electron happens extraordinarily fast. By a rough estimate on the excitation time in *K* edge XAS, it was shown to be much faster than the vibrational state. This guarantees the XAS to be an effective tool to capture the instantaneous information of the structure and the chemical bonding of the systems.

1.3.2 Core-Hole Creation

The absorption of a photon can result in excitation of a core electron depending on the energy of the photon as shown in Figure 1.3. In the X-ray absorption process the incident X-ray photon is absorbed and a core electron is excited into an unoccupied state. For the higher energy photon which is larger than the core electron ionization potential, the electron is removed from the molecule (transferred to the continuum of states given by a free electron in the presence of a core-hole potential).

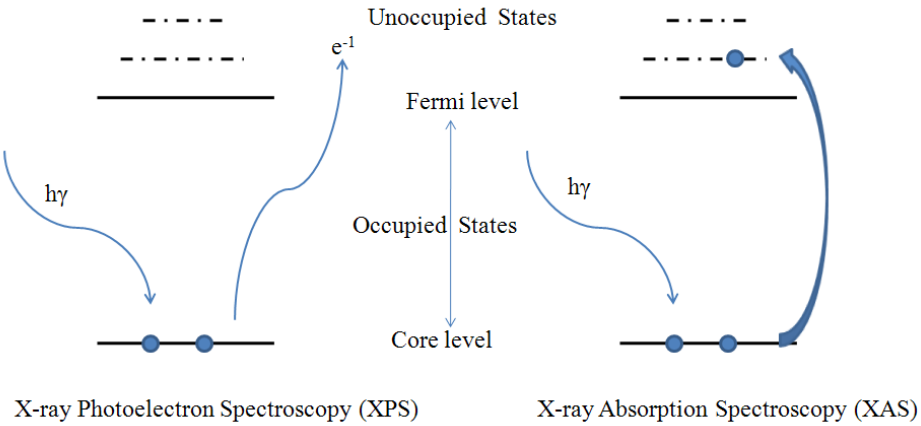

Fig. 1.3 Schematic display of the core hole ionization process in X-ray photoelectron spectroscopy (XPS) and X-ray absorption spectroscopy (XAS).

The consequence of the core-hole creates an attractive coulomb potential around the absorbing atom. Thus, the system will of course respond to this potential to find the lowest energy configuration in the presence of the core hole. For free molecules this generally means contraction of orbitals at the excited site, whereas neighboring molecules are polarized.

1.3.3 Core-Hole Decay

As discussed above, the core-hole creation processes produce an excited final state which is unstable to electronic and nuclear relaxation. And this induces spontaneous electronic transitions to fill the core-hole, i.e. the core-hole decay processes which can be classified into radiant decay and non-radiant decay, schematically described in Figure 1.4. If an electron from the occupied band transits into the core hole with a photon emitted, this is radiant decay and is called X-ray emission spectroscopy (XES). In another case, the non-radiant decay, hence no photon is involved. There will be two valence holes together with an ejected electron, the Auger electron. Measurements of the ejected electron energy distribution form the basis for Auger Electron Spectroscopy (AES).

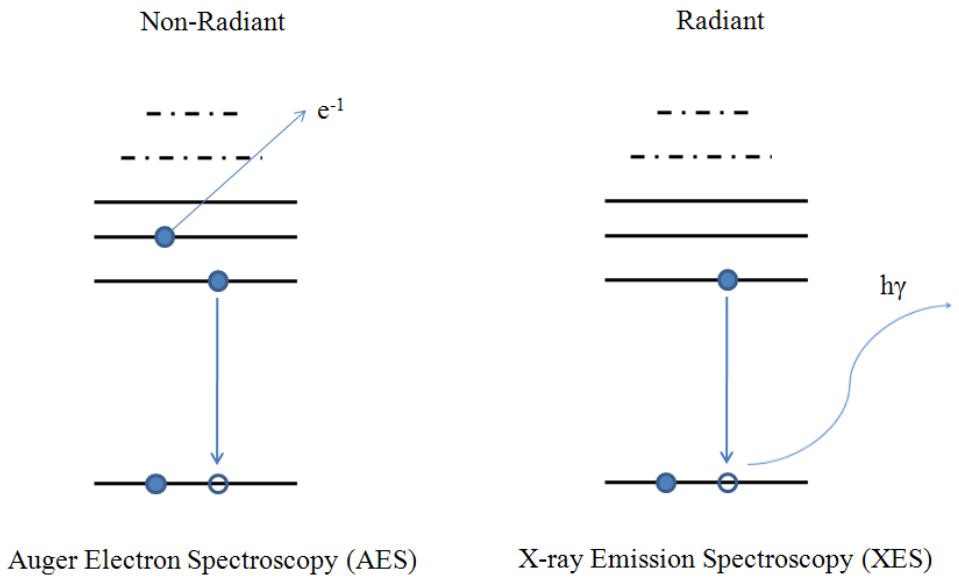

Fig. 1.4 Schematic picture of core-hole decay process in Auger Electron Spectroscopy (AES) and X-ray emission spectroscopy (XES).

Core level spectroscopy is intrinsically affected by the core-hole lifetime broadening, which gives a finite energy width to the energy levels. As we all know, energy levels have a precise sharply defined energy only if the states last for an infinitely long period; anything limits their lifetime introduces a broadening to the spectral features. An atom with a core hole is in an excited, unstable state. It has a finite lifetime because electrons in higher energy states rapidly make transitions to fill the core hole, either emitting fluorescence radiation in the process, or undergoing non-radiative decay. Generally, the core-hole lifetime which is determined by the number of electrons that can lower their energy with a probability directly related to their overlap with the core-hole wavefunction is a nearly pure atomic property and is shorter for deep core levels. The Heisenberg uncertainty relation implies that the finite lifetime τ produces an uncertainty (broadening) of the energy $\Delta E \approx \hbar/\tau$.

1.4 The motivation and the organization of this thesis

Motivation

Ice physics study dates back to more than 100 years ago and there still exist many ambiguities. Experimental challenges associated with low temperatures/slow kinetics and weak scattering intensity of hydrogen atoms complicates the comparison between experiments and theoretical calculations. With the help of advanced *ab initio* computations, we attempt to focus on theoretical investigation on the hydrogen bond network in ice XIII which is the most complicated ice phases observed so far.

Core level spectroscopy is believed to be a powerful tool in probing the local chemical environments around the excited sites and this is due to the fact that XAS is

site specific.[36] It has also been shown recently that similar agreements with X-ray diffraction (XRD) and neutron diffraction data show insensitivity to the different configurations, in particular in the hydrogen bond involved materials[37-40] which also drives search for the new experimental tool to probe hydrogen bond environments. In this thesis, we demonstrated that oxygen *K* edge XAS is an effective structural tool to distinguish the similar hydrogen bond configurations. Furthermore, there are still many ambiguities and controversies between experiments and theoretical literatures which need to be solved, especially in the interpretation of the pre-edge feature. With the aim of shedding some light on this controversial issue, we calculated the oxygen *K* edge XAS in all the crystalline phases of ice serving a good model since ice structures are commonly established.

Recently, H_2-H_2O attracts a lot attention based on the fact that it is regarded as the potential medium for hydrogen storage and it has important implications for the astrophysics. Under compression, phase transitions were investigated using XRD and Raman spectroscopy.[41,42] In the low pressure region, C_2 hydrogen hydrate remains a cubic crystal structure and the structural transitions were observed at approximately 35-40 and 55-60 GPa and the high-pressure phase can survive up to at least 80.3 GPa.[42] However, these two high-pressure phases are not yet determined by the experiments and this drives us to look at the structural and vibrational properties with DFT methods.

Organization

In this thesis, we demonstrated that the DFT could capture the ground state in the ice system successfully as illustrated in ice XIII and then we systematically study the

oxygen *K* edge XAS in different crystalline phases. Furthermore, we carried out molecular dynamics study on the ice-relating material, H_2-H_2O, to examine its structural changes, vibrational properties, and H-bond symmetrization under compression and 300 K. We start from chapter 2 with introduction to the methodology employed in this thesis. In chapter 3, we combine the graph theory and the DFT to locate the ground state structure of ice XIII. Oxygen *K* edge XAS in ice system was discussed in chapter 4. First principle molecular dynamics study on H_2-H_2O under compression was given in chapter 5. Last is the conclusion and future work section in chapter 6.

1.5 References:

(1) Bartels-Rausch, T.; Bergeron, V.; Cartwright, J. H. E.; Escribano, R.; Finney, J. L.; Grothe, H.; Gutierrez, P. J.; Haapala, J.; Kuhs, W. F.; Pettersson, J. B. C.; Price, S. D.; Sainz-Diaz, C. I.; Stokes, D. J.; Strazzulla, G.; Thomson, E. S.; Trinks, H.; Uras-Aytemiz, N. *Reviews of Modern Physics*, *84*, 885.

(2) Salzmann, C. G.; Radaelli, P. G.; Mayer, E.; Finney, J. L. *Physical Review Letters* **2009**, *103*.

(3) Stillinger, F. H. *Science* **1980**, *209*, 451.

(4) Buckingham, A. D.; Del Bene, J. E.; McDowell, S. A. C. *Chemical Physics Letters* **2008**, *463*, 1.

(5) Latimer, W. M.; Rodebush, W. H. *Journal of the American Chemical Society* **1920**, *42*, 1419.

(6) Luzar, A.; Chandler, D. *Physical Review Letters* **1996**, *76*, 928.

(7) Kumar, R.; Schmidt, J. R.; Skinner, J. L. *Journal of Chemical Physics* **2007**, *126*.

(8) Giauque, W. F.; Ashley, M. F. *Physical Review* **1933**, *43*, 81.

(9) Giauque, W. F.; Stout, J. W. *Journal of the American Chemical Society* **1936**, *58*, 1144.

(10) Pauling, L. *Journal of the American Chemical Society* **1935**, *57*, 2680.

(11) Bramwell, S. T.; Gingras, M. J. P. *Science* **2001**, *294*, 1495.

(12) Tajima, Y.; Matsuo, T.; Suga, H. *Nature* **1982**, *299*, 810.

(13) Jackson, S. M.; Nield, V. M.; Whitworth, R. W.; Oguro, M.; Wilson, C. C. *Journal of Physical Chemistry B* **1997**, *101*, 6142.

(14) Wang, Y.; Li, J. C.; Kolesnikov, A. I.; Parker, S.; Johnsen, S. J. *Physica B* **2000**, *276*, 282.

(15) Buch, V.; Sandler, P.; Sadlej, J. *Journal of Physical Chemistry B* **1998**, *102*, 8641.

(16) Whalley, E.; Heath, J. B. R.; Davidson, D. W. *Journal of Chemical Physics* **1968**, *48*, 2362.

(17) Londono, J. D.; Kuhs, W. F.; Finney, J. L. *Journal of Chemical Physics* **1993**, *98*, 4878.

(18) Johari, G. P.; Lavergne, A.; Whalley, E. *Journal of Chemical Physics* **1974**, *61*, 4292.

(19) Kuhs, W. F.; Finney, J. L.; Vettier, C.; Bliss, D. V. *Journal of Chemical Physics* **1984**, *81*, 3612.

(20) Salzmann, C. G.; Radaelli, P. G.; Hallbrucker, A.; Mayer, E.; Finney, J. L. *Science* **2006**, *311*, 1758.

(21) Bernal, J. D.; Fowler, R. H. *Journal of Chemical Physics* **1933**, *1*, 515.

(22) Berendsen, H. J. C.; Grigera, J. R.; Straatsma, T. P. *Journal of Physical Chemistry* **1987**, *91*, 6269.

(23) Jorgensen, W. L.; Chandrasekhar, J.; Madura, J. D.; Impey, R. W.; Klein, M. L. *Journal of Chemical Physics* **1983**, *79*, 926.

(24) Sanz, E.; Vega, C.; Abascal, J. L. F.; MacDowell, L. G. *Physical Review Letters* **2004**, *92*.

(25) Car, R.; Parrinello, M. *Physical Review Letters* **1985**, *55*, 2471.

(26) Kuo, J. L.; Coe, J. V.; Singer, S. J.; Band, Y. B.; Ojamae, L. *Journal of Chemical Physics* **2001**, *114*, 2527.

(27) Kuo, J. L.; Klein, M. L. *Journal of Physical Chemistry B* **2004**, *108*, 19634.

(28) Kuo, J. L.; Singer, S. J. *Physical Review E* **2003**, *67*.

(29) Singer, S. J.; Kuo, J. L.; Hirsch, T. K.; Knight, C.; Ojamae, L.; Klein, M. L. *Physical Review Letters* **2005**, *94*.

(30) Lokshin, K. A.; Zhao, Y. S.; He, D. W.; Mao, W. L.; Mao, H. K.; Hemley, R. J.; Lobanov, M. V.; Greenblatt, M. *Physical Review Letters* **2004**, *93*.

(31) Mao, W. L.; Mao, H. K. *Proceedings of the National Academy of Sciences of the United States of America* **2004**, *101*, 708.

(32) Mao, W. L.; Mao, H. K.; Goncharov, A. F.; Struzhkin, V. V.; Guo, Q. Z.; Hu, J. Z.; Shu, J. F.; Hemley, R. J.; Somayazulu, M.; Zhao, Y. S. *Science* **2002**, *297*, 2247.

(33) Patchkovskii, S.; Tse, J. S. *Proceedings of the National Academy of Sciences of the United States of America* **2003**, *100*, 14645.

(34) Vos, W. L.; Finger, L. W.; Hemley, R. J.; Mao, H. K. *Physical Review Letters* **1993**, *71*, 3150.

(35) Vos, W. L.; Finger, L. W.; Hemley, R. J.; Mao, H. K. *Chemical Physics Letters* **1996**, *257*, 524.

(36) Stöhr, J. *NEXAFS Spectroscopy*; Springer-Verlag: Berlin, 1992.

(37) Soper, A. K. *Journal of Physics-Condensed Matter* **2005**, *17*, S3273.

(38) Leetmaa, M.; Wikfeldt, K. T.; Ljungberg, M. P.; Odelius, M.; Swenson, J.; Nilsson, A.; Pettersson, L. G. M. *The Journal of Chemical Physics* **2008**, *129*, 084502.

(39) Wikfeldt, K. T.; Leetmaa, M.; Ljungberg, M. P.; Nilsson, A.; Pettersson, L. G. M. *Journal of Physical Chemistry B* **2009**, *113*, 6246.

(40) Iannuzzi, M. *Journal of Chemical Physics* **2008**, *128*, 204506.

(41) Hirai, H.; Ohno, S.; Kawamura, T.; Yamamoto, Y.; Yagi, T. *Journal of Physical Chemistry C* **2007**, *111*, 312.

(42) Machida, S.; Hirai, H.; Kawamura, T.; Yamamoto, Y.; Yagi, T. *Journal of Chemical Physics* **2008**, *129*.

Chapter 2

In this chapter, a brief introduction of the first principle quantum theory for the material calculations is presented. Density functional theory (DFT) has become the most popular method for theoretical study in condensed matter physics. In this thesis, we used DFT for the total energy calculation, X-ray absorption spectra simulation in ice and the molecular dynamics study in the H_2-H_2O under pressure.

First Principles Quantum Theory

2.1 Born-Oppenheimer approximation

The exact Hamiltonian of a system with *N* electrons and *K* nuclei with charges Z_n is

$$H = \sum_{i=1}^{N} \frac{p_i^2}{2m} + \sum_{n=1}^{K} \frac{P_n^2}{2M_n} + \frac{1}{4\pi\varepsilon_0}\frac{1}{2}\sum_{i,j=1;i\neq j}^{N} \frac{e^2}{\left|\vec{r}_i - \vec{r}_j\right|} - \frac{1}{4\pi\varepsilon_0}\sum_{n=1}^{K}\sum_{i=1}^{N} \frac{Z_n e^2}{\left|\vec{r}_i - \vec{R}_n\right|} + \frac{1}{4\pi\varepsilon_0}\frac{1}{2}\sum_{n,n'=1;n\neq n'}^{K} \frac{Z_n Z_{n'} e^2}{\left|\vec{R}_n - \vec{R}_{n'}\right|} \quad (2.1)$$

where *i* is noted as the electrons and *n* as the nuclei, *m* is the electron mass, and M_n are the masses of different nuclei. The first two terms represent the kinetic energies of electrons and nuclei respectively while the third term represents the Coulomb

repulsion between electrons and nuclei while the fourth term represents Coulomb attraction between electrons and nuclei; the fifth term is the Coulomb repulsion between the nuclei.

To solve the stationary Schrödinger equation, approximation must be made since the above Hamiltonian is too complicated for the systems (number of electrons and nuclei is larger than four) even on the most powerful computer available. The proton or neutron is about 1835 times as large as the electron mass, so it is clear that the nuclei moves much more slower than the electrons. It is reasonable to separate the movements of the nuclei from the electrons which is known as the Born-Oppenheimer approximation. In this case, electrons adopt themselves in the field generated by a static configuration of nuclei. The Born-Oppenheimer Hamiltonian for the electrons is

$$H_{BO} = \sum_{i=1}^{N} \frac{p_i^2}{2m} + \frac{1}{4\pi\varepsilon_0}\frac{1}{2}\sum_{i,\,j=1;i\neq j}^{N} \frac{e^2}{\left|\vec{r}_i - \vec{r}_j\right|} - \frac{1}{4\pi\varepsilon_0}\sum_{n=1}^{K}\sum_{i=1}^{N} \frac{Z_n e^2}{\left|\vec{r}_i - \vec{R}_n\right|} \tag{2.2}$$

The nuclei are treated on a classical level since the ground state is determined as the minimum of their potential energy, neglecting quantum fluctuations. The problem of solving the electronic wave functions using the Hamiltonian remains intractable even by fixing the nuclei positions because too many degrees of freedom are involved.

2.2 Density functional theory (DFT)

There are more and more DFT applications in the material modeling nowadays.

2.2.1 Hohenberg-Kohn theorem

Hohenberg-Kohn (HK) theorem is the foundation of the DFT.[1] The remarkable importance of the HK theorem is that it simply avoids to deal directly interacting many electrons to study the ground state properties of a system. It solves many-body problem consisting N electrons from 3N spatial coordinates to 3 spatial coordinates and this open a new way to study the electronic system.

The theory which was originally proposed by Hohenberg and Kohn are usually given in the following three statements.

Statement 1 (Uniqueness): The ground state expectation value of any observable is a unique functional of the exact ground state density *n(r)*.

Statement 2 (Variational Principle): The exact ground state density minimizes the total energy functional *E[n]*.

Statement 3 (Universality): The functional F[n] is universal in the sense that it does not depend on $V_{ext}(\vec{r})$.

$$E_n = F_n + \int d^3\vec{r} V_{ext}(\vec{r}) n(\vec{r}) \tag{2.3}$$

2.2.2 Kohn-Sham equation

In the Hartree-Fock formalism, it consists of approximating the N-electron wavefunction by an anti-symmetrized product of N one-electron wave functions for the solutions of the many body Schrödinger equation. This product is usually referred to a Slater determinant

$$\Psi(x_1, x_2, \cdots x_N) = (N!)^{-1/2} \begin{vmatrix} \psi_1(x_1) & \psi_2(x_1) & \cdots & \psi_N(x_1) \\ \psi_1(x_2) & \psi_2(x_2) & \cdots & \psi_N(x_2) \\ \vdots & \vdots & & \vdots \\ \psi_1(x_N) & \psi_2(x_N) & \cdots & \psi_N(x_N) \end{vmatrix}. \qquad (2.4)$$

However, the nonlocal character which caused by the dependence of the Hartree-Fock equations to the occupied electron orbitals limits its application to the solids.[2] Solving the many interacting particles is notoriously difficult. The attraction of DFT is that it facilitates to approximate this many-body system calculations without the construction of many-body wave functions. Instead, one could extract the needed information from a one-body quantity, the density.[3] DFT is a successful approach for the description of ground state properties of many-electron system.

In DFT, we adopt an effective independent-particle Hamiltonian resulting in the following Schrödinger equation:

$$H_{BO} = \sum_{i=1}^{N} \frac{p_i^2}{2m} + \frac{1}{4\pi\varepsilon_0}\frac{1}{2}\sum_{i,j=1;i\neq j}^{N} \frac{e^2}{|\vec{r}_i - \vec{r}_j|} - \frac{1}{4\pi\varepsilon_0}\sum_{n=1}^{K}\sum_{i=1}^{N} \frac{Z_n e^2}{|\vec{r}_i - \vec{R}_n|}$$

$$[\sum_{i=1}^{N}\frac{p_i^2}{2m}+\frac{1}{4\pi\varepsilon_0}\frac{1}{2}\sum_{i,j=1;i\neq j}^{N}\frac{e^2}{|\vec{r}_i-\vec{r}_j|}-\frac{1}{4\pi\varepsilon_0}\sum_{n=1}^{K}\sum_{i=1}^{N}\frac{Z_n e^2}{|\vec{r}_i-\vec{R}_n|}+V_{xc}[n](\vec{r})]\psi_k(\vec{r})=\varepsilon_k\psi_k(\vec{r})$$

(2.5)

The first three terms are kinetic energy, the electrostatic interaction between electrons and the nuclei, and the electrostatic energy of the electrons feeling the potential by the total electron density $n(\vec{r}')$. The fourth term is an exchange-correlation potential containing the many-body effects. The beauty of the DFT is that it could yield exact ground state energy if we know the form of exchange-correlation potential. Unfortunately, this exact form is unknown, but there exist several approximations. The solution of equation must be in a self-consistent way and the density is

$$n(\vec{r})=\sum_{k=1}^{N}|\psi_k(\vec{r})|^2 \qquad (2.6)$$

where the sum is over the N spin-orbitals $\psi_k(\vec{r})$ whose lowest eigenvalues is ε_k and N is the number of the total electrons in the system.

The total energy is given by

$$E=\sum_{k=1}^{N}\varepsilon_k-\frac{1}{2}\int d^3r d^3r' r' n(\vec{r})\frac{1}{|\vec{r}-\vec{r}'|}n(\vec{r}')+E_{xc}[n]-\int d^3r V_{xc}[n](\vec{r})n(\vec{r}) \qquad (2.7)$$

where the exchange correlation potential $V_{xc}[n]$ is the functional derivative of this energy with respect to the density:

$$V_{xc}[n](\vec{r}) = \frac{\delta}{\delta n(\vec{r})} E_{xc}[n] \tag{2.8}$$

Equation (2.5) are solved in an iterative self-consistency loop which is started by choosing an initial density $n(\vec{r})$, constructing the Kohn-Sham equation from it, solving the latter and calculating the resulting density from expression (2.6). Then a new Schrödinger equation is constructed and so on, until the density does not change appreciably any more.

2.2.3 Pseudopotentials

Most of the physical properties are determined by the valence electrons to a much larger extent compared with the bounded core electrons. In this circumstance, the pseudopotential approximation is proposed as an effective potential for the systems. One condition is imposed that the valence wavefunction has to be orthogonal to the core wavefunction. The valences electrons are represented by nodeless pseudo wavefuctions while the core electrons are assumed to be together with nuclei as ion core. In the norm-conserving scheme, the eigenstates of the pseudo-wavefunction and all electron wavefunction are the same beyond a certain cutoff radius r_c. The larger the r_c, the softer the pseudopotential, that is faster to converge while less transferable.

2.2.4 Local density approximation (LDA)

The exact expression for the exchange correlation functional is not known and it is a functional of density. In practice, we need to use approximations for the E_{xc}. For a

nonhomogenous system, the exchange correlation functional at position $\vec{r}$ depends on the density value at $\vec{r}$ and its variation near to $\vec{r}$. Therefore, we could deduce the expression as an expansion of the density gradients to arbitrary order:

$$V_{xc}[n](\vec{r}) = V_{xc}[n(\vec{r}), \nabla n(\vec{r}), \nabla(\nabla n(\vec{r})), ...] \quad (2.9)$$

Further approximation is made by assuming that the exchange correlation potential rely solely on the density at $\vec{r}$ —this is the so called local density approximation (LDA)[4-6]:

$$E_{xc}^{LDA} = \int d^3 r \varepsilon_{xc}(n(\vec{r}))n(\vec{r}) \quad (2.10)$$

where $\varepsilon_{xc}(n)$ is the exchange correlation energy per particle of an homogenous electron gas at density n. Obviously, LDA is exact for the homogenous electron gas. Since LDA does not include the dependence on gradient of the density, the accuracy of the LDA differs case by case. If the density does not change much in the material, the accuracy would be sufficient high. Because LDA solely determined by local density, it is a short range potential and reduces exponentially. Nonetheless, LDA gains great successes even in some inhomogeneous systems.

Beside the good results obtained with LDA, it also shows its limitations and insufficiency to describe the density variation. For example, LDA underestimates lattice constant while overestimates bulk moduli. Considering this, better description of the exchange correlation function to include higher order density gradient are motivated.

2.2.5 Generalized gradient approximation (GGA)

Generalized gradient approximation (GGA) was born with taking the first order density gradient into account.

$$E_{xc}^{GGA} = \int d^3 r n(\vec{r}) f(n, |\nabla n|) \tag{2.11}$$

where f(n, |∇n|) is function tuned to guarantee good performance of GGA in different conditions. It is known that GGA is superior to LDA in most cases and hence people adopted GGA more often in the modern DFT simulaitons.[7-14]

2.2.6 Plane Wave basis set

There are many advantages to adopt the plane wave basis set, i.e. applicable to all atomic species and easy to arrive completeness convergence.

The potential of a periodic system is

$$V(\vec{r} + n\vec{a}) = V(\vec{r}) \tag{2.12}$$

in which $\vec{a}$ is lattice vector and n is an integer. As stated in Bloch's theorem

$$\psi_i(\vec{r}) = e^{i\vec{k}\cdot\vec{r}} f_i(\vec{r})$$

$$f_i(\vec{r}) = \sum_{\vec{G}} c_i \vec{G} e^{i\vec{G}\cdot\vec{r}} \tag{2.13}$$

$$\psi_i(\vec{r}) = \sum_{\vec{G}} c_i \vec{G} e^{i(\vec{k}+\vec{G})\cdot\vec{r}}$$

where $\vec{G}$ is a reciprocal lattice vector.

2.3 DFT applications to the X-ray absorption spectra calculation

Concerning the experimental limitations of X-ray absorption spectroscopy (XAS) measurements, like the bulk penetration problem and saturation effects[15], it is essential and important to study the XAS theoretically. DFT[1,16] is an exact theory for ground state calculation. Recently, there are enormous applications to use the DFT as an approximate approach to study the excitation physics. In this thesis, we also adopted

the DFT method to calculate the XAS in ice system. The electrons are relaxed self-consistently and the excitation energies are calculated with the so called ΔSCF method[4,17,18]. Another method proposed by Slater[19] is the transition state method. In this method, half core electron is excited to the unoccupied state. It needs to be noted that the transition state method is just a numerical approximation of the ΔSCF method since there is no half electron in reality. In practice, direct implementation of these two methods needs to calculate all the excited states and this is unrealistic.

The full core hole (FCH) or half core hole (HCH) model is a more practical choice in which full or half core electron is promoted in the excited atom while the excited electron was eliminated.[20,21] HCH is believed to have good performance in small molecules and clusters calculations while FCH gain much success in condensed phase materials[20-25] which is also confirmed in our work as discussed in Chap. 4. Moreover, half occupation used in HCH is somehow random and empirical. From this point of view, we could adjust this fractional occupation to achieve agreements with experimental data without deeper understanding the problem.

2.3.1 Electronic Dipole Approximation

The interactions between the incident photons and the matter are intrinsically the electromagnetic fields of the incident photons coupled with the electrons and nuclei of the matter itself. The electric fields will induce the oscillations of the electrons and nuclei, hence form electric dipoles.

The absorption cross section from the initial state $|i>$ to final state $|f>$ derived from the time-dependent perturbation theory:

$$\sigma_{abs} = \sum_f \frac{4\pi^2\hbar}{m_e\omega}\frac{e^2}{\hbar c}\left|\left\langle f\left|e^{\frac{i\omega}{c}\vec{n}\cdot\vec{x}}\vec{\varepsilon}\cdot\vec{p}\right|i\right\rangle\right|^2 \delta(E_f - E_i - \hbar\omega) \tag{2.12}$$

Here, ω is the electromagnetic field frequency; E_i and E_f represent the energies of the initial and final configuration, respectively, $\vec{\varepsilon}$ is the polarization vector while $\vec{n}$ is field transmitted direction. Considering ω/c =2π/λ, the Taylor expansion series

$$e^{\frac{i\omega}{c}\vec{n}\cdot\vec{r}} = 1 + \frac{i\omega}{c}\vec{n}\cdot\vec{r} + \cdots \approx 1 \tag{2.13}$$

Generally, the electromagnetic field wavelength is much larger than the size of the radiated atom. Thus, (2.13) can be truncated by its leading term 1 while neglecting the higher order terms. This is the so called electronic dipole approximation. The electronic dipole approximation is proved to be valid and efficient in the XAS study. An electronic dipole could be used to describe the electro-magnetic fields:

As a result, equation (2.12) becomes

$$\left\langle f\left|e^{\frac{i\omega}{c}\vec{n}\cdot\vec{r}}\vec{\varepsilon}\cdot\vec{p}\right|i\right\rangle \approx \vec{\varepsilon}\left\langle f\left|\vec{p}\right|i\right\rangle \tag{2.14}$$

Using the commentator relations:

$$\begin{aligned} &[\vec{r}, H_0] = \frac{i\hbar\vec{p}}{m_e} \\ &\left\langle f\left|\vec{p}\right|i\right\rangle = \frac{m_e}{i\hbar}\left\langle f\left|[\vec{r}, H_0]\right|i\right\rangle = im_e\omega_{fi}\left\langle f\left|\vec{r}\right|i\right\rangle \end{aligned} \tag{2.15}$$

where $\omega_{fi} = (E_f - E_i)/\hbar$.

Summing up all the possible final state and suppose that the polarization direction is x axis and we then have:

$$\sigma_{abs}=\sum_f \frac{4\pi^2\alpha_0\hbar}{m_e^2\omega}\left|\langle f|p_x|i\rangle\right|^2\delta(\omega-\omega_{fi})=\sum_f 4\pi^2\alpha_0\hbar\omega\left|\langle f|x|i\rangle\right|^2\delta(\omega-\omega_{fi}) \quad (2.16)$$

Here $\alpha_0=\frac{e^2}{\hbar c}\approx\frac{1}{137}$ is the fine structure constant.

Using the commentator relations:

$$[x,[x,H_0]]=-\frac{\hbar^2}{m_e} \quad (2.17)$$

Thus,

$$\langle i|[x,[x,H_0]]|i\rangle=\langle i|x^2H_0+H_0x^2-2xH_0x|i\rangle=-\frac{\hbar^2}{m_e} \quad (2.18)$$

giving

$$2\sum_f(\langle i|x|f\rangle E_i\langle f|x|i\rangle-\langle i|x|f\rangle E_f\langle f|x|i\rangle)=-\frac{\hbar^2}{m_e} \quad (2.19)$$

Then

$$\frac{2m_e}{\hbar}\sum_f\omega_{fi}\left|\langle f|x|i\rangle\right|^2=1 \quad (2.20)$$

and this is the Thomas-Reiche-Kuhn sum rule. We could deduce that it is needed to normalize the spectra by integrating the spectral shape with respect to the energy range and this also facilitates the comparison in difference circumstances.

To ensure the observable XAS transition, we have to guarantee $\langle f|x|i\rangle\neq 0$ in equation (2.16) and this requires $\Delta l=\pm1,\Delta m=0$ (l is orbital angular momentum quantum number and m is the quantum number of the orbital angular momentum projection along the x-axis). This is the selection rule derived from the electric dipole transitions. For the *K*-edge XAS, only the *s*→*p* transitions are allowed in the electric dipole

approximation. Actually, there exist forbidden transitions, like *s*→*s* transitions, while at a much lower possibility than the allowed ones. The magnetic dipole transitions caused by the interaction between the electron spin and the magnetic fields of the incident photons happen on a less $1/10^5$ times rate than the electric dipole transitions while the electric quadrupole transitions ($\Delta l = 0,\pm 2$) happens happen on a less $1/10^8$ times rate compared with electric dipole transitions.

2.3.2 XAS formalism implemented in Wien2k code

Neckel and Schwarz[26-29] proposed a way to calculate XAS in the framework of augmented plane wave (APW) methods. In the formula, the *K* edge XAS intensity $I_A^0(E)$ for atom A is given by:

$$I_A^0(E) \propto E^3 M_A^2(p,1s,\varepsilon)\chi_p^A(\varepsilon) \tag{2.21}$$

with the corresponding L_2, L_3, M_2, or M_3 spectrum is given by

$$I_A^0(E) \propto E^3[M_A^2(s,n'p',\varepsilon)\chi_s^A(\varepsilon) + \frac{2}{5}M_A^2(d,n'p',\varepsilon)\chi_d^A(\varepsilon)] \tag{2.22}$$

in which $E-\varepsilon-\varepsilon_{core}$ corresponds to energy of the outgoing X-rays, the $\chi_l^A(\varepsilon)$ term represents the local *l*-type density of states of the unoccupied states at energy ε , and $M_A^2(l,n'l',\varepsilon)$ denotes the radial transition matrix from the conduction state of energy ε and *l*-like wavefunctions to a core hole states *n'l'* at energy ε_{core} in which *n'*=2 for L_2, L_3; *n'*=3 for M_2, M_3; *l'*=1 referred to *p*. The transition matrix $M_A^2(l,n'l',\varepsilon)$ obey the dipole selection rule $\Delta l = \pm 1$ and E^3 contribution is from the Dirac theory on radiation.

2.3.3 Molecular orbital picture

The free water molecule has a simple geometric structure where oxygen atom forms two covalent bonds to two hydrogen atoms. The water molecular orbitals are denoted according to the C_{2v} point group symmetry with the following ground state configuration

$(1a_1)^2(2a_1)^2(1b_2)^2(3a_1)^2(1b_1)^2$

$1a_1$ is the localized O 1*s* core orbital, and the $2a_1$ is the inner valence orbital with mainly O 2*s* character. The outer valence consists of the strongly bonding $1b_1$ orbital, the non-bonding lone-pair orbital $1b_2$, and the $3a_1$ which has both bonding and lone-pair character. In the unoccupied valence region, the mixing of O 2*p* and H 1*s* gives the two OH anti-bonding combinations, $4a_1$ and $2b_2$ orbitals.

2.3.4 More accurate approaches to calculate XAS

Time Dependent Density Functional Theory (TDDFT) is a theory which has been mathematically established by the theorem of Runge and Gross[30]. Basically, it is an extension of the conventional ground-state DFT to deal with time-dependent external perturbations. The time-dependent external potential drives the system away from its stationary ground-state to higher energy levels. TDDFT has wide applications in calculating the optical spectra.

In many-body perturbation theory, the optical spectra are obtained by solving Bethe-Salpeter equation (BSE). An optical absorption of photon produces an interacting electron-hole pair, names as exciton. The BSE has successful applications to calculate the optical spectra of insulators, semiconductors, atoms, clusters.

2.4 *Ab initio* molecular dynamics

Molecular dynamics (MD) is a widely used methods by the integrating the equation of motion (2.22) numerically for a large collection of particles.

$$\frac{d^2\vec{r}_i(t)}{dt^2} = \frac{F_i(R)}{m_i}$$
$$F_i(R) = \sum_{\substack{j=1.,N;\\ j\neq i}} F(|\vec{r}_i - \vec{r}_j|)\vec{r}_{ij} \qquad (2.23)$$

R denotes the position coordinates $\vec{r}_i$ of all particles, m_i is the mass of the particle i. The forces between particles are unknown. Usually, the forces are determined from *ab initio* simulations (first principle MD) or empirical models by fitting the experimental data (classical MD). The great advantage of the MD method is that it not only provides a way to evaluate expectation values of static physical quantities, but also the dynamical phenomena, such as transport of heat or charge, and relaxation of systems far from equilibrium.

2.5 References

(1) Hohenberg, P.; Kohn, W. *Physical Review B* **1964**, *136*, B864.

(2) Pisany, C.; Dovea, R.; Roetti, C. *Hartree-Fock Ab-initio treatment of crystalline systems*; Springer: Berlin, 1988.

(3) Baroni, S.; de Gironcoli, S.; Dal Corso, A.; Giannozzi, P. *Reviews of Modern Physics* **2001**, *73*, 515.

(4) Jones, R. O.; Gunnarsson, O. *Reviews of Modern Physics* **1989**, *61*, 689.

(5) Langreth, D. C.; Mehl, M. J. *Physical Review Letters* **1981**, *47*, 446.

(6) Perdew, J. P.; Zunger, A. *Physical Review B* **1981**, *23*, 5048.

(7) Ahuja, R.; Eriksson, O.; Wills, J. M.; Johansson, B. *Physical Review B* **1996**, *53*, 3072.

(8) Ernzerhof, M.; Perdew, J. P.; Burke, K. Density functionals: Where do they come from, why do they work? In *Density Functional Theory I*, 1996; Vol. 180; pp 1.

(9) Perdew, J. P.; Burke, K. *International Journal of Quantum Chemistry* **1996**, *57*, 309.

(10) Perdew, J. P.; Burke, K.; Ernzerhof, M. *Physical Review Letters* **1996**, *77*, 3865.

(11) Perdew, J. P.; Burke, K.; Ernzerhof, M. Local and gradient-corrected density functionals. In *Chemical Applications of Density-Functional Theory*; Laird, B. B., Ross, R. B., Ziegler, T., Eds., 1996; Vol. 629; pp 453.

(12) Perdew, J. P.; Burke, K.; Wang, Y. *Physical Review B* **1996**, *54*, 16533.

(13) Perdew, J. P.; Emzerhof, M.; Burke, K. *Journal of Chemical Physics* **1996**, *105*, 9982.

(14) Perdew, J. P.; Yue, W. *Physical Review B* **1986**, *33*, 8800.

(15) Myneni, S.; Luo, Y.; Naslund, L. A.; Cavalleri, M.; Ojamae, L.; Ogasawara, H.; Pelmenschikov, A.; Wernet, P.; Vaterlein, P.; Heske, C.; Hussain, Z.; Pettersson, L. G. M.; Nilsson, A. *Journal of Physics-Condensed Matter* **2002**, *14*, L213.

(16) Kohn, W.; Sham, L. J. *Physical Review* **1965**, *140*, 1133.

(17) Hellman, A.; Razaznejad, B.; Lundqvist, B. I. *Journal of Chemical Physics* **2004**, *120*, 4593.

(18) Gavnholt, J.; Olsen, T.; Engelund, M.; Schiotz, J. *Physical Review B* **2008**, *78*.

(19) Slater, J. C.; Johnson, K. H. *Physical Review B* **1972**, *5*, 844.

(20) Triguero, L.; Pettersson, L. G. M.; Agren, H. *Physical Review B* **1998**, *58*, 8097.

(21) Buczko, R.; Duscher, G.; Pennycook, S. J.; Pantelides, S. T. *Physical Review Letters* **2000**, *85*, 2168.

(22) Rez, P.; Alvarez, J. R.; Pickard, C. *Ultramicroscopy* **1999**, *78*, 175.

(23) Tanaka, I.; Araki, H.; Yoshiya, M.; Mizoguchi, T.; Ogasawara, K.; Adachi, H. *Physical Review B* **1999**, *60*, 4944.

(24) Lie, K.; Hoier, R.; Brydson, R. *Physical Review B* **2000**, *61*, 1786.

(25) Elsasser, C.; Kostlmeier, S. *Ultramicroscopy* **2001**, *86*, 325.

(26) Neckel, A.; Schwarz, K.; Eibler, R.; Weinberger, P.; Rastl, P. *Berichte Der Bunsen-Gesellschaft-Physical Chemistry Chemical Physics* **1975**, *79*, 1053.

(27) Schwarz, K.; Neckel, A. *Berichte Der Bunsen-Gesellschaft-Physical Chemistry Chemical Physics* **1975**, *79*, 1071.

(28) Schwarz, K.; Neckel, A.; Nordgren, J. *Journal of Physics F-Metal Physics* **1979**, *9*, 2509.

(29) Schwarz, K.; Ripplinger, H.; Neckel, A. *Zeitschrift Fur Physik B-Condensed Matter* **1982**, *48*, 79.

(30) Runge, E.; Gross, E. K. U. *Physical Review Letters* **1984**, *52*, 997.

Chapter 3

In this chapter, we combined density functional theory and graph theory to locate the ground-state of ice XIII which is the most complicated ice phase having been observed so far. It turned out that the experimentally refined structure is one of the lowest enthalpy structures (most stable ones) as calculated with density functional theory.

Ground state prediction of hydrogen bond network in ice XIII under compression

3.1 Introduction

The phase diagram of water is very complex and has been experimentally obtained with at least sixteen crystalline phases so far. Lately, Salzmann *et al*[1] has synthesized two new phases of ice, which were named after ice XIII and XIV, respectively. Actually, it is not an easy job to compare among experiments since there exists a number of experimental challenges associated with low temperatures-slow kinetics, low scattering cross section for hydrogen atoms, and difficulties in mapping out the phase line between different phases.. On the theoretical side, the underlying insight of ice has been investigated through empirical potentials [2-5] and more recently,

there is a growing trend on the application of first principles methods.[6-10] In all these obtained crystalline phases of ice, oxygen atoms must have tetrahedral coordination, but the hydrogen atoms may be disordered or ordered subject to the constraint of "ice rules"[11]. Hence, the largest challenge for the theoretical study of ice is the generation of all the possible configurations which need to follow the restrictions listed above and this is proved to be a huge number. . Although a number of empirical models[4,12] have successfully reproduced the complicated phase diagram of water, they showed their inability to capture the hydrogen disordered-ordered transition sequence[13]. Instead of using an empirical model, very recently, the structure of ice XIV was predicted by Tribello *et al*[6] based on density functional theory (DFT) calculations and they suggested two or more metastable, proton ordered structures of ice XIV.

According to the powder neutron diffraction[1], ice XIII, the proton-ordered counterpart of ice V, has a primitive monoclinic cell comprising 28 molecules with 7 crystallographically symmetry different oxygen positions. The highest symmetry space group of ice XIII from the observed diffraction pattern is $P2_1/a$ and this is a sub-group of A2/a, space group of ice V. So far, ice XIII becomes the most complicated ice phase among the obtained sixteen phases. Knight *et al*[14] studied hydrogen bond fluctuations and proton ordering thermodynamics in ice V and XIII using statistical mechanical methods focusing on the phase transition along the temperature scale. In this work, we are motivated to investigate the pressure influences on the electronic structure and bonding properties. Here, we employed

ice-rule-allowed configurations enumeration scheme [15,16], which has been successfully applied to ice Ih[17], ice VII/VIII[18,19], and ice VI[20] in our previous works. We found that the experimentally proposed fully ordered structure is energetically competitive in this work due to the the relative enthalpy in the geometry optimization. In our case, all atomic positions and lattice box are fully relaxed until the energy threshold reaches no more than 1×10^{-6} eV per atom between the optimization cycle steps in contrast with Knight *et al*[14] who only optimized atomic positions but not the cell parameters. We utilized a Monkhorst-Pack[21] $2\times2\times2$ grid of *k*-points and a plane wave energy cutoff that it is one of the lowest enthalpy structures of the given ice XIII phase identified by DFT.

3.2 Computation methods

We started by exploring all the possible hydrogen-bonding configurations for ice XIII allowed by the ice rule in a unit cell of 28 water molecules. Considering the comparably large size of the unit cell (28 water molecules) and the low symmetry of its monoclinic space group, we finally arrived at 69380 structures after removed the duplicate ones. This complexity makes the prediction of the proton ordered phase and the analysis of its properties challenging and formidable. To reduce the number of structures for geometry optimization calculations and since it has been speculated that the proton ordered phase should have maximal symmetry[6], we only consider the high symmetry configurations. Therefore, only 70 structures are selected for following enthalpy calculations; these fall into two main groups classified by different space

group $P2_1/a$ and Cc. Each structure was fully relaxed and the relative enthalpies[22] (H=E+PV) were caclulated using the plane wave code VASP[23]. We adopted the PAW formalism potential[24] using both generalized gradient approximations (GGA) PW91[25] functional and local density approximation (LDA) and an energy cutoff 520 eV to guarantee the convergence and reliability of our simulation results. We increased the *k*-points grid up to 4×4×4 in the DOS calculation with the tetrahedron method for better analyzing electronic structure.

3.3 Results and discussions

The relative stability of these 70 selected high-symmetry structures at 0 GPa was depicted in Fig. 3.1.First, we would like to evaluate the contribution of zero point energy to the total energy qualitatively. We found very small variation in the volume of the relaxed cells and the OH bond length variance less than 0.0021Å and the O-O variance is 0.024Å. Consequently, the geometry of these configurations is almost identical, which indicates that the vibration modes (and hence the phonon sum and therefore the zero point energy) would be expected to be almost identical for each configuration. Therefore, it is safe to arrive at the conclusion that the contribution from the zero point energy is negligible between these closely related ice networks and the energy differences are principally dominated by the electrostatic interaction. The experimentally observed proton ordered structure is one of our DFT predicted lowest enthalpy configurations regardless of the exchange-correlation functional, which shows the energetic competitiveness and reliability of our methodology. We

could see that these two space group symmetry structures scattered and mixed up together. In other words, no difference of low-enthalpy result calculated by LDA and GGA was observed here. The overall trend in the stability is quite similar for LDA and GGA, even though the fitted line still deviates from the diagonal line; we attribute this minor discrepancy to the difference existing in LDA and GGA. It is surprising to find out that LDA that could not reproduce the geometry of water molecule well arrived at same trend with GGA functional. This implies that the exchange-correlation functional does not play an important role on the observed difference in total enthalpy. Therefore, by analysis of the DFT total energy formula we may speculate that the total enthalpy differences relate to the electrostatic interaction. From this, we can further deduce that the physical mechanism behind the proton ordering can be attributed to a mainly electrostatic interactions also suggested by Tribello *et al*[26].

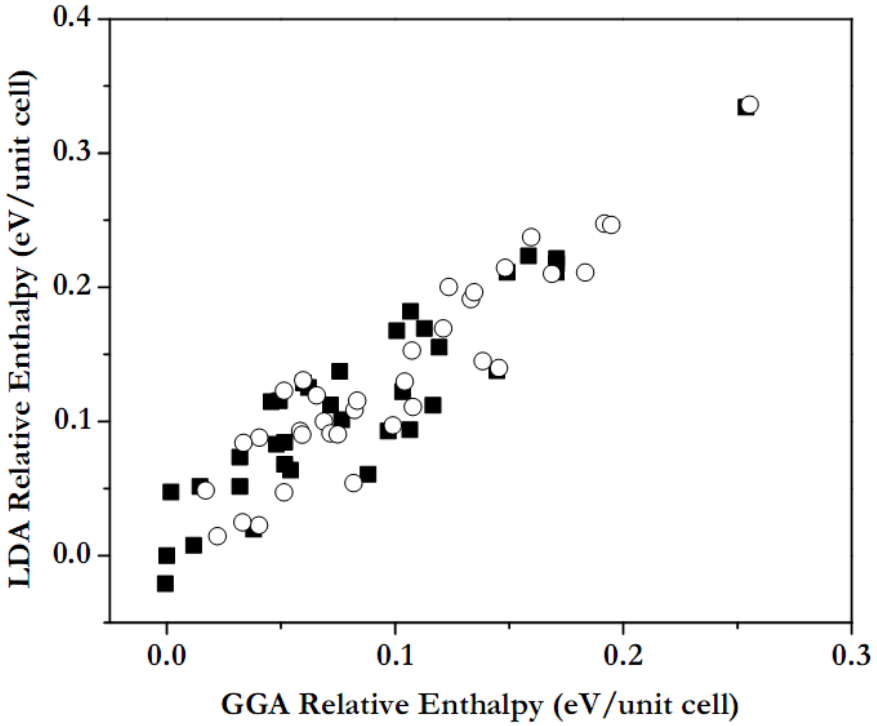

Fig. 3.1 Relative enthalpy (eV/unit cell) to the experimental ice XIII structure calculated by LDA and GGA of 70 selected structures. The solid squares and empty circles representing structures with space group P21/a and CC, respectively.

From Fig. 3.1, however, we still can see some structures occasionally reverting in stability within these two exchange-correlation functionals, but there is a group of structures clearly lying near the true ground state. The small energetic difference makes it impossible to distinguish by DFT which one is the most stable structure. In the following, we chose four lowest-enthalpy (most stable) structures as displayed in Fig. 3.2 from the GGA results. It is known that the P21/a symmetry group has inversion symmetry and thus dipole moment in these four structures is zero. The enthalpy difference between these four configurations is sufficiently small (less than 10^{-4} eV/water) that one would expect all these four configurations to be observed. In particular, configuration (a) has the same structure as the experimentally observed proton ordered structure[1]. We also double checked the relative enthalpy of these four

structures with a larger k-point mesh (3×3×3) and higher plane wave cutoff (700 eV) in the optimization. All the evidences supported our prediction of energetic robustness of these four structures. Since cooling rate and strain[27] can affect the phase and the proportions of different phases, it is also reasonable that there exist lowest enthalpy configurations that are metastable forms of ice XIII which are formed under kinetically controlled conditions.

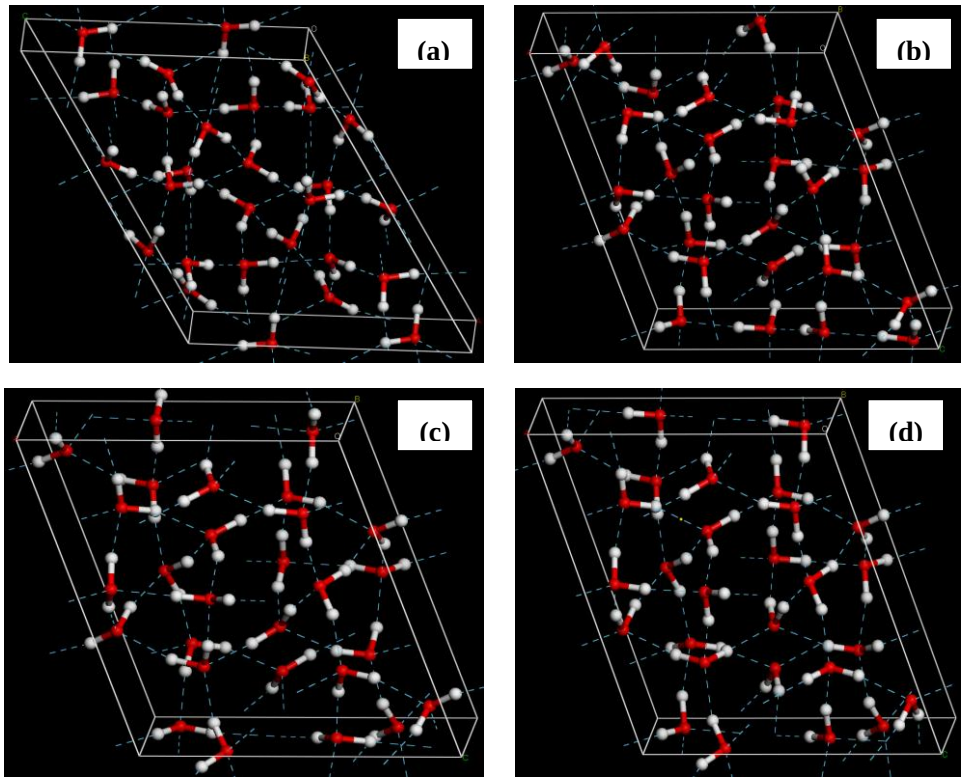

Fig. 3.2 Four predicted lowest enthalpy structures in which (a) is equivalent to the experimental structure in reference 2. The red and white balls represent oxygen and hydrogen atoms, respectively, and the light blue dashed lines represent hydrogen bonds.

Recently, it has been shown that some distorted hydrogen bonds environments could have indistinguishable X-ray (XRD) and neutron diffraction data.[28-31] Simulated XRD

and neutron diffraction data from the PowderCell 2.3 code[32] with λ= 1.540598 Å which supports the structure determination using powder diffraction data are displayed in Fig. 3.3 and Fig. 3.4. We could infer that both XRD and neutron diffraction patterns are hardly distinguishable and the characteristic peak (2-13) as a sign of the ordered phase is observed in all these four structures.

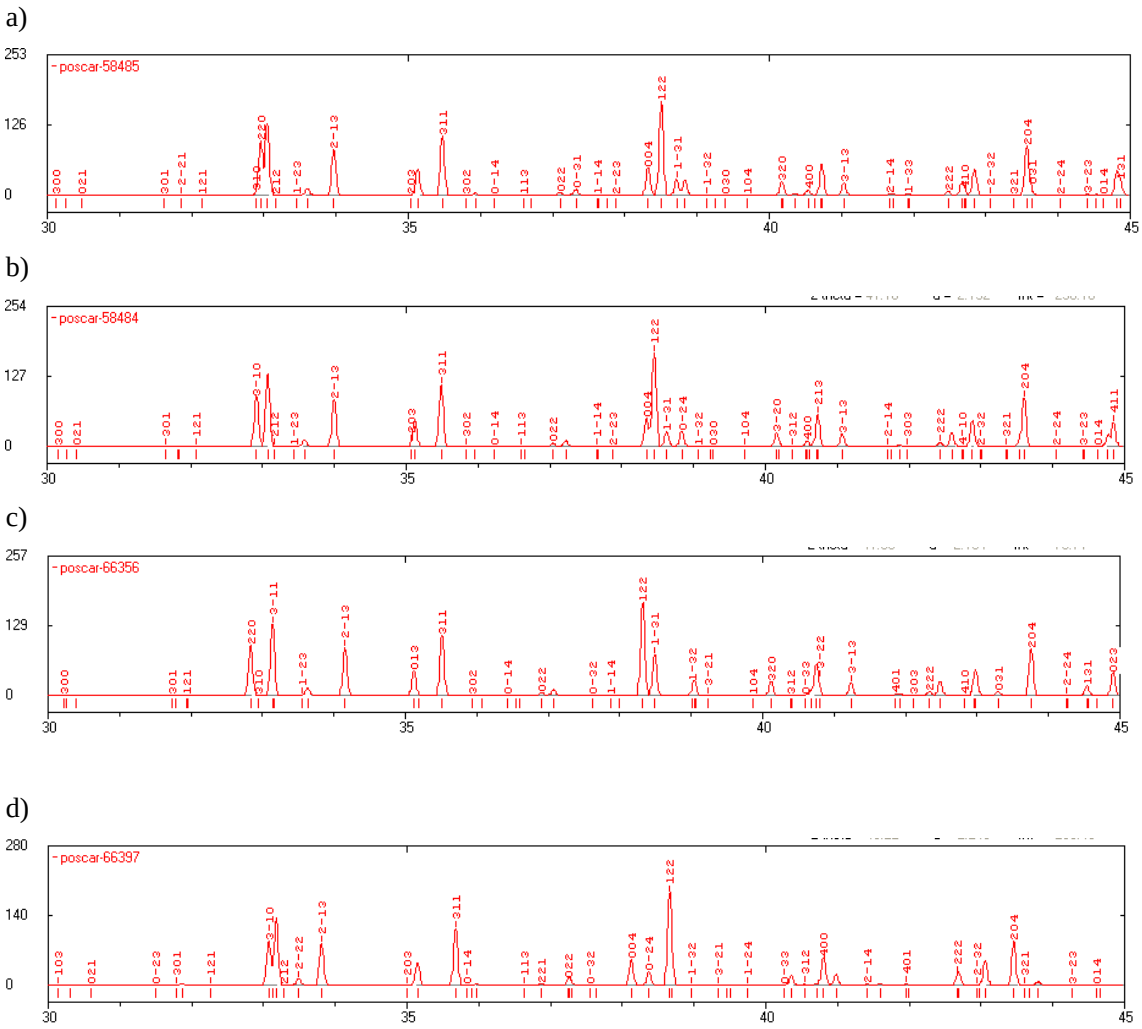

Fig. 3.3 Simulated XRD patterns of the four structures (a-d) listed in Fig. 3.2.

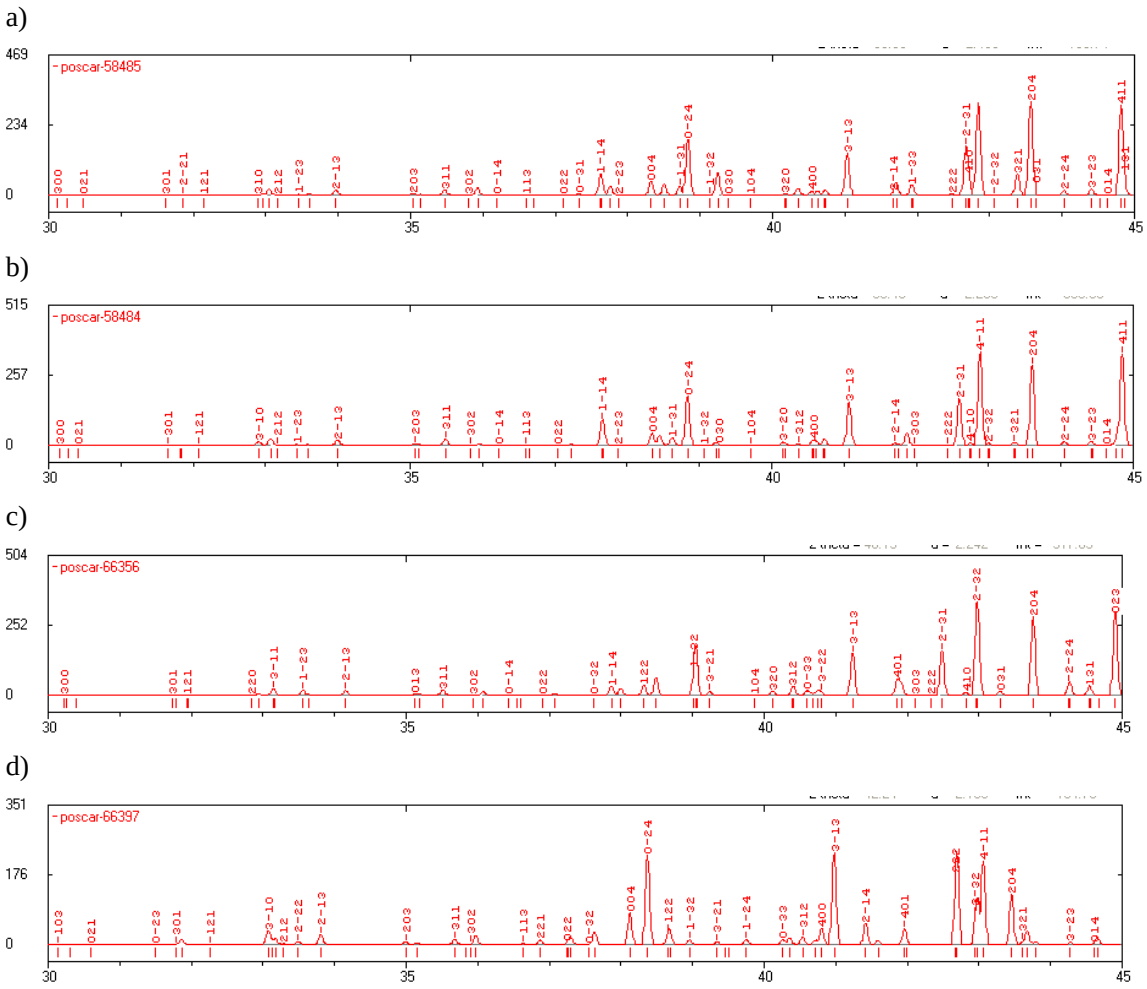

Fig. 3.4 Simulated neutron diffraction patterns of the four structures (a-d) listed in Fig. 3.2.

In next chapter, we will focus on this set of low-enthalpy structures and investigate their electronic absorption features in the oxygen *K* edge XAS at ambient pressure with the purpose to provide helpful insights into the local structure in these configurations. Oxygen *K* edge XAS spectra with standard deviation obtained by averaging over different oxygen sites are plotted in Figure 4.7.

3.4 Conclusions

In this work, we have used DFT to investigate hydrogen bond network in ice XIII under compression. We demonstrated that DFT methods have successfully reproduced the experimentally found structure. However, a few low-enthalpy metastable states are likely to co-exist from the total enthalpy calculation results. This is reasonable due to the fact that the dopants type and its concentration may have significant influence on the formation of these phases.

3.5 References

(1) Salzmann, C. G.; Radaelli, P. G.; Hallbrucker, A.; Mayer, E.; Finney, J. L. *Science* **2006**, *311*, 1758.

(2) Aragones, J. L.; Noya, E. G.; Abascal, J. L. F.; Vega, C. *The Journal of Chemical Physics* **2007**, *127*, 154518.

(3) Mahoney, M. W.; Jorgensen, W. L. *The Journal of Chemical Physics* **2000**, *112*, 8910.

(4) Sanz, E.; Vega, C.; Abascal, J. L. F.; MacDowell, L. G. *The Journal of Chemical Physics* **2004**, *121*, 1165.

(5) Mahoney, M. W.; Jorgensen, W. L. *Journal of Chemical Physics* **2000**, *112*, 8910.

(6) Tribello, G. A.; Slater, B.; Salzmann, C. G. *J. Am. Chem. Soc.* **2006**, *128*, 12594.

(7) Hamann, D. R. *Physical Review B* **1997**, *55*, 10157.

(8) Klug, D. D.; Tse, J. S.; Liu, Z. X.; Gonze, X.; Hemley, R. J. *Physical Review B* **2004**, *70*, 144113.

(9) Tse, J. S.; Klug, D. D. *Physical Review Letters* **1998**, *81*, 2466.

(10) Umemoto, K.; Wentzcovitch, R. M.; Baroni, S.; de Gironcoli, S. *Physical Review Letters* **2004**, *92*, 105502.

(11) Bernal, J. D.; Fowler, R. H. *The Journal of Chemical Physics* **1933**, *1*, 515.

(12) Martin-Conde, M.; MacDowell, L. G.; Vega, C. *Journal of Chemical Physics* **2006**, *125*.

(13) Buch, V.; Sandler, P.; Sadlej, J. *The Journal of Physical Chemistry B* **1998**, *102*, 8641.

(14) Knight, C.; Singer, S. J. *The Journal of Chemical Physics* **2008**, *129*, 164513.

(15) Knight, C.; Singer, S. J.; Kuo, J.-L.; Hirsch, T. K.; Ojamae, L.; Klein, M. L. *Physical Review E (Statistical, Nonlinear, and Soft Matter Physics)* **2006**, *73*, 056113.

(16) Kuo, J.-L.; Coe, J. V.; Singer, S. J.; Band, Y. B.; Ojamae, L. *The Journal of Chemical Physics* **2001**, *114*, 2527.

(17) Kuo, J.-L.; Klein, M. L.; Kuhs, W. F. *The Journal of Chemical Physics* **2005**, *123*, 134505.

(18) Kuo, J.-L. *Physical Chemistry Chemical Physics* **2005**, *7*, 3733.

(19) Kuo, J. L.; Klein, M. L. *J. Phys. Chem. B* **2004**, *108*, 19634.

(20) Kuo, J. L.; Kuhs, W. F. *J. Phys. Chem. B* **2006**, *110*, 3697.

(21) Monkhorst, H. J.; Pack, J. D. *Physical Review B* **1976**, *13*, 5188.

(22) Tribello, G. A.; Slater, B.; Salzmann, C. G. *Journal of the American Chemical Society* **2006**, *128*, 12594.

(23) Kresse, G.; Hafner, J. *Physical Review B* **1993**, *47*, 558.

(24) Blöchl, P. E. *Physical Review B* **1994**, *50*, 17953.

(25) Perdew, J. P.; Chevary, J. A.; Vosko, S. H.; Jackson, K. A.; Pederson, M. R.; Singh, D. J.; Fiolhais, C. *Physical Review B* **1992**, *46*, 6671.

(26) Tribello, G. A.; Slater, B. *Chemical Physics Letters* **2006**, *425*, 246.

(27) Line, C. M. B.; Whitworth, R. W. *Journal of Chemical Physics* **1996**, *104*, 10008.

(28) Soper, A. K. *Journal of Physics-Condensed Matter* **2005**, *17*, S3273.

(29) Leetmaa, M.; Wikfeldt, K. T.; Ljungberg, M. P.; Odelius, M.; Swenson, J.; Nilsson, A.; Pettersson, L. G. M. *The Journal of Chemical Physics* **2008**, *129*, 084502.

(30) Wikfeldt, K. T.; Leetmaa, M.; Ljungberg, M. P.; Nilsson, A.; Pettersson, L. G. M. *Journal of Physical Chemistry B* **2009**, *113*, 6246.

(31) Iannuzzi, M. *Journal of Chemical Physics* **2008**, *128*, 204506.

(32) http://www.ccp14.ac.uk/ccp/web-mirrors/powdcell/a_v/v_1/powder/e_cell.html.

Chapter 4

In this chapter, we calculated the oxygen *K* edge X-ray absorption spectra in ice systematically and extensively by means of density functional theory. Before the production calculations in different crystalline phases, we tested the spectra dependence on supercell size, exchange-correlation functional, and the different model (full core hole and half core hole). We found that the pre-edge is a universal feature in these different crystalline ice phases except ice X while the main spectra difference lies in the main peak area (~537-540 eV). In combination with the electronic density of states analysis, the pre-edge is caused by oxygen 1*s*-4a_1 transitions and the main peak is due to the oxygen 1*s*-2b_2 transitions. The disappearance of the pre-edge feature in ice X could be explained as the perfect tetrahedral symmetry removes the *p* character from the 4a_1 orbitals, hence, no transition intensity in the pre-edge followed by the dipole selection rule.

On the Sensitivity of Oxygen *K* Edge X-ray Absorption Spectra to Hydrogen Bond Topology in Different Crystalline Phases of Ice: A Density Functional Theory Study

4.1 Introduction

Understanding hydrogen bonding is essential for a complete understanding of the

phenomenon in a number of physical, chemical, and biological studies of the hydrogen bond related issues[1-5] In spite of extensive research both in experiments and theoretical simulation over last several decades, it still remains an elusive goal to give out a clear picture to interpret the hydrogen bonding. Recently, X-ray absorption spectroscopy (XAS) which would be the oxygen near *K* edge measurements in water system has been applied to examine the structure of water. That mainly relies on the principles that XAS is very sensitive to probe the unoccupied states which could excite individual atom and hence can shed light on the instantaneous local environments of the absorbing oxygen atom.[6]

The structure of water is widely accepted as tetrahedrally coordination as in ice and this model has been questioned recently.[7] Intensive debate over the structure model for liquid water has been ongoing, especially on the percentage of the broken hydrogen bonds (H-bonds) and no unambiguous conclusion is reached so far[7-19]. By analyzing the oxygen *K* edge XAS, the authors speculated[7] that large percentage of broken H-bond presented in liquid water and this induces the chain structure rather than the conventional tetrahedral model. The proof of this proposal comes from the strong pre-edge feature as observed in liquid water which is similar to the case in water surface. In the latter one, the surface area is obviously rich in broken H-bond. To reinforce this conclusion, the authors[7] carried out theoretical calculations based on water cluster model and they suggested that the observed spectral features can be explained only if the structure of water includes a large number of non-coordinated water molecules. This new hypothesis which is in conflict with the

conventional concept that water has mainly tetrahedral coordination has stimulated active experimental and theoretical re-examinations later on.

Smith *et al.*[14] measured oxygen *K* edge XAS in supercooled and normal liquid water droplets and found that the absorption spectra features strongly depended on the temperature. From this, they determined the energy required for H-bonds rearrangement in liquid water. They pointed out that the energy measured just matches the latent heat of melting of ice I_h and agrees with the distribution of H-bonds calculated from tetrahedrally arranged water molecules as derived from simulations using the ST2 model of water. Head-Gordon *et al*[17] supported the tetrahedral model evidenced the long range correlations obtained from X-ray scattering pattern and hence proved the chain structure to be invalid. Moreover, double donor H-bond configurations do contribute to pronounced pre-edge peaks as the single donor H-bond and non H-bond molecule in liquid water with transition state theory reported by Wang *et al*.[15] Very recently, Tse *et al.*[10] observed the pre-edge feature in high density amorphous ice, low density amorphous ice, ice Ih, normal and deuterated liquid water using X-ray Raman scattering spectra (XRS). Their work brought out the doubt on taking pre-edge feature to measure the fraction of the broken H-bond. Furthermore, a previous XRS[20] study of ice II, III, and IX linked pre-edge feature with proton ordering and a recent study[21] related the spectral feature with structural changes in the second coordination shell or even higher coordination shells[22]. All in all, to date, there is little consensus on the Oxygen *K* edge XAS in aqueous system.

It is important to note that there exist difficulties in the experimental techniques on XAS, such as attenuation depth of X-ray above the oxygen *K* edge of smaller than one micron, saturation effects, and also the ion/electron yield measurements are surface sensitive and vacuum condition is compulsory[23]. Therefore, to gain a complete interpretation of the water XAS relies on comparing with the calculated spectra. It is well accepted that each water molecule is connected to four neighboring water molecules through H-bonds. The structurally well-characterized ice phases can act as valuable model systems for studying the connection between local structure and XAS spectral features. Recently, there is a XAS theoretical report through solving the approximate Bethe-Salpeter equation[19,24] (BSE) which bears overall close agreement with experiment, however, underestimated the pre-edge intensity both in ice I_h and water. The authors have ignored the core hole dynamics and used a static Coulomb-hole and screened exchange approximation to calculate the self-energy. Core spectroscopy was calculated with modern GW-BSE theoretical method in water and ice systems which get resasonable agreement with experimental while a systematic narrow width is present.[24] BSE describes the electron excitations process from perturbation theory and it involves two-particle interaction. This leads to very cumbersome calculations because a four-point equation relating to these two particles' evolution needs to be solved. BSE is essential for the optical excitations dealing with valence orbitals while calculating XAS is much less complicated since the energy of core electrons is very isolated, as indicated in the recent review papers[25] and references therein which also claimed the success of applying transition potential

DFT to study the XAS in ice and water. Also, J. J. Rehr[26] showed that for deep core XAS, BSE and the final state rule (Half core hole (HCH) and full core hole (FCH)) are closely similar and P. Blaha[27] also confirmed this DFT core-hole calculations result in fairly accurate results for *K* edges XAS. As we all know, ice has a very intricate phase diagram[28]. So far, to our best knowledge, there is no systematic theoretical report on oxygen *K* edge XAS in different ice phases. Consequently, in view of the experimental uncertainties, attempts for systematic theoretical investigations on the oxygen *K* edge XAS in various H-bond geometries in different crystalline ice phases were motivated with the aim to gain deeper insight into the controversial issue mentioned above. We found that the pre-edge feature exists in the ice system except ice X while the main spectra distinctness occurs in the main peak region indicating its great sensitivity to the local H-bond environments. Furthermore, we probed the origin of spectral features in oxygen *K* edge XAS in terms of *s* and *p*-type projected density of states (PDOS). This special capability allows a detailed view of the unoccupied electronic structure and chemical bonding.

4.2 Computation methods

Theoretical calculations of oxygen *K* edge XAS were based on full-potential linearized augmented plane wave method (LAPW) + local orbitals method implemented in the WIEN2k package[29,30] which is very reliable when dealing with nano-materials and crystals.[31-33] We adopted a supercell approximation with 1*s* core electron occupation to be 1 which was believed to be a popular and successful methods for the core-level spectroscopy calculations. The supercell approximation

adopted here was on the purpose to isolate the interaction between excited oxygen atoms. In the calculation, generalized gradient approximations (GGA) PBE[34] for exchange-correlation functional was used and $R_{mt}*K_{max}$= 5 was set. The Monkhorst-Pack scheme[35] with symmetry was applied for a Brillouin zone integration of each supercell. We relaxed the valence electrons in a self-consistent manner. Calculated oxygen *K* edge XAS was obtained using Fermi golden rule and is calculated from the transitions allowed by dipole selection, generating transition matrix elements and then are multiplied with a radial transition probability and also the PDOS.[36,37] HCH/FCH models are realized through removing a half/full core electron of the excited oxygen atom. To guarantee the charge neutrality, we used a charged background under periodic boundary conditions.[16] For comparison with experiments, we have broadened the theoretical spectra with a Lorentzian of full width at half maximum FWHM = 1.0 eV. The absolute energy scale of the calculated XAS was determined by shifting the spectra to coincide with the first excitation energy to ease the comparison with experiments, keeping in mind that our calculated XAS spectra focus on the shape only (relative position of the peaks and spectral distributions). To ease the comparison with experimental data, X-ray absorption sum rule was normalized by integrating absorption intensities from 530 eV to 550 eV for all the spectra.

4.3 Results and discussions

4.3.1 Benchmark calculations on the *K* edge XAS

Firstly, we carried out the investigations of the core-hole influences in a series materials consisting of six first row elements (excluding oxygen and neon) with full core hole approach. There are only K edge XAS for the first row elements. We compared our calculated XAS with experimental data in Fig. 4.1.We indicated conduction band minimum as zero in the figure and the experimental spectra[38] are vertically aligned for comparison. It can be seen that there is a very satisfactory agreement between the simulated spectra and the experimental ones in these six crystals and this gives us confidence for applying this method to calculate the oxygen K edge XAS in ice system.

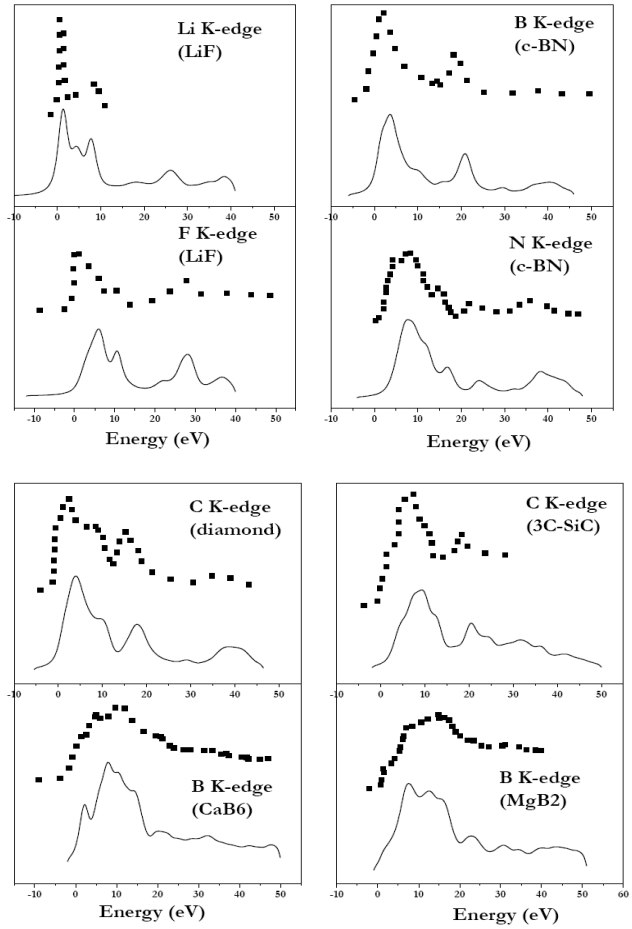

Fig. 4.1 Comparison of simulated XAS with full core hole approach (solid lines) and experimental data (solid squares) in these six materials (LiF, C-BN, diamond, 3C-SiC, CaB_6, and MgB_2).

4.3.2 Oxygen *K* edge XAS in ice

In this thesis, we studied the oxygen *K* edge XAS in different ice crystalline phases in combination with the oxygen atom *s-p* hybridization and molecular orbital distribution of the probed molecule. For proton ordered phases, the structures (ice II[39], V[40], VIII[41], IX[42], X[43], XI[44], and partial ordered phase XII[40]) are established with the help of experimental refinement data. For proton disordered phases, theoretical oxygen *K* edge XAS were calculated with the ground state (most stable) configuration obtained

by enumerating all the possible configurations satisfying ice rules. The detailed scheme has been introduced and applied to different ice phases in our previous studies[45-51]. In the calculated unit cell, there exists more than one crystalgraphically distinct oxygen atom, the calculated spectra lines were obtained by weight averaging on all distinct oxygen sites.

The choice of computational method to compute XAS in aqueous systems has been actively discussed recently[9,16,52-55]. We found that the calculated spectra of ice I_h without a core hole failed to reproduce the experimental spectra, which highlights the importance of considering core hole effects in the excitation simulation in the ice systems. Because of the most available experimental data on ice I_h, we first benchmarked the influences of the FCH/HCH and the exchange correlation functional on the oxygen *K* edge XAS spectra of ice I_h and the results are shown in Fig. 4.2. Here, we used a 96 atoms supercell to speed up the calculation and this choice definitely does not affect the conclusion summarized from this test. One can easily find that all the experimental features were well reproduced in our calculation. Generally, the absorption spectra is classified into three regions: pre-edge (around 535 eV), main peak (537-540 eV), and post-edge (from 540 eV onwards).[7] From the left panel of Fig. 4.2, one can see that the calculated results

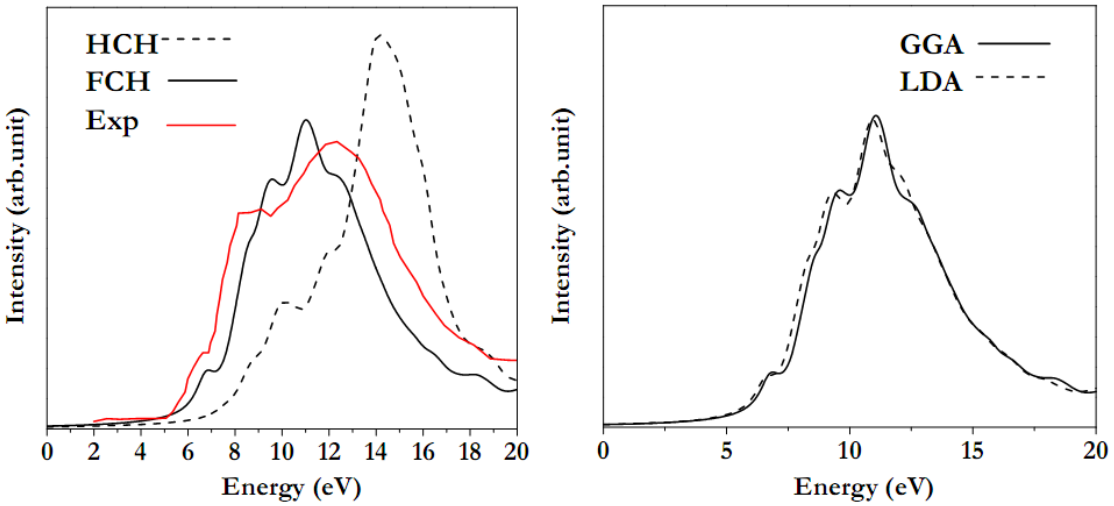

Fig. 4.2 Left: Comparison of calculated oxygen *K* edge XAS in ice I_h containing 96 atoms with different models for the X-ray absorption process, viz HCH and FCH. Right: A similar comparison between different exchange correlation functional, GGA and LDA.

are in good agreements with experimental data with FCH showing closer agreement with the experimental results than HCH. In comparison, HCH potential has the trend to enhance the post-edge region and it could not reproduce the pre-edge feature well which is of important concern. HCH is believed to perform pretty well in small molecules and clusters while FCH is more preferred in solids calculations[56-61]. Hetényi *et a.l*[16] carried out XAS simulations in ice with relaxed Kohn-Sham excitations and compared the spectra obtained from FCH and HCH. The authors proved that FCH could give better description of XAS. From the right panel of Fig. 4.2, we found that there is negligible effect with the choice of exchange correlation functional using generalized gradient approximation (GGA) and local density approximation (LDA). Since GGA is believed to provide better description of the H-bonded materials[62-64], hence, GGA and FCH were employed in the following calculations.

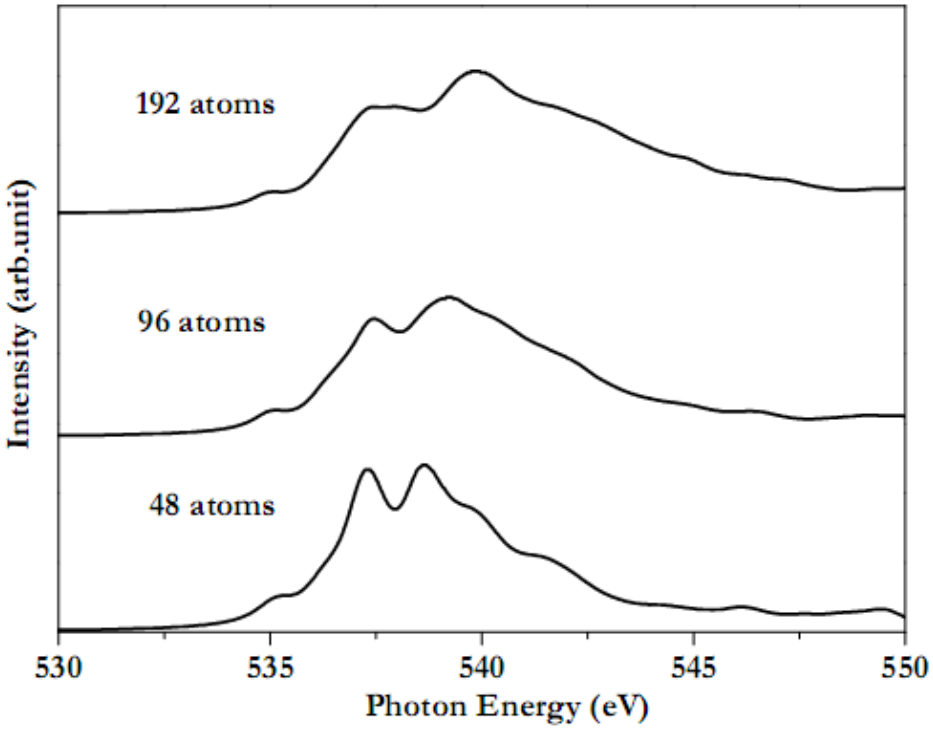

Fig. 4.3 Dependence on supercell size of calculated oxygen *K* edge XAS on ice Ih with FCH and GGA functional.

Secondly, to illustrate the importance of the supercell size, we show the size dependence of the oxygen *K* edge XAS in ice I_h in Fig. 4.3 calculated with the scheme outlined above. We obtained an excellent agreement with experimental result using FCH for a sufficiently large unit cell size (64 water molecules) and a good agreement, with all features reproduced semi-quantitatively, for a 32 water molecules cell while a poorly reproduced spectra for a too small supercell with 16 water molecules only; The key point concluded from the supercell test is that it takes a supercell of more than 100 atoms for the spectrum to converge. Moreover, order of 10^2 atoms in a supercell approach in band structure codes was also recommended by J. J. Rehr.[65] A small supercell contributes to the inaccuracy both in the peak positions and in the relative

intensities of the peaks. For ice I_h, I_c, II, III, IV, V, VI, VII, VIII, IX, X, XI, and XII, the supercell size is 192, 192, 216, 144, 192, 168, 120, 192, 192, 144, 162, 192, and144 atoms, respectively. The choice of supercell size here is a compromise between computational cost and accuracy. The minimum distances for the exicited centers (core-hole) in each structure are all larger than 10Å to ensure the reliability of the simulation, which are much larger than 6Å proposed by Chris J. Pickard et al[38]. As displayed in Fig. 4.4, the agreement between the experimental and calculated XAS on ice I_h with 192 atoms supercell is very satisfactory with all features quantitatively reproduced. It should be noted that these two experiments used different techniques, XAS and X-ray Raman scattering (XRS), respectively. Moreover, we could extract same information from XRS and XAS under the dipole approximation.[66,67] XRS is a more advanced since it has stronger penetration ability and could be measured for small cross section in extreme circumstances . Relative intensity of pre-edge to main-edge, and also to post-edge varies are different before the two experiments due to the saturation effects. These discrepancies between different experiments show the difficulties in the measurements of absolute intensity of XAS which was also suggested in Ref. 10. The good agreement with experimental spectra supports the validity of current theoretical model and gives us

further confidence in the following XAS calculations in the other ice phases.

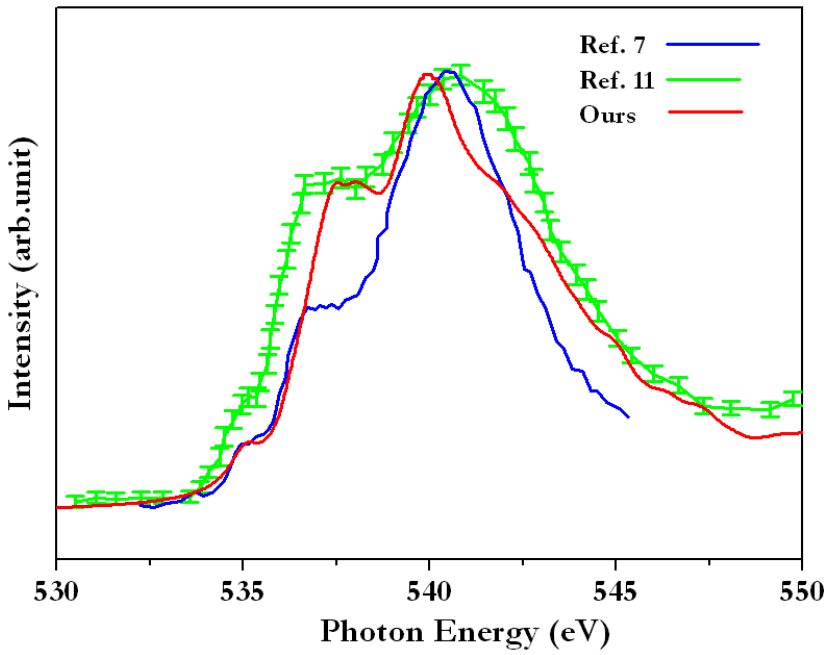

Fig. 4.4 Comparison of calculated oxygen *K* edge XAS on ice Ih with experimental data, in which the blue and red solid line are from Ref. 7 (XAS) and Ref. 10 (XRS), respectively.

Similar features of oxygen *K* edge XAS have also been observed in the other phases of ice as displayed in Fig. 4.5 and the error bars are obtained as the standard deviation by exciting different oxygen atoms. We found that the distinct pre-edge in the oxygen *K* edge XAS is a common feature appearing in all the ice crystalline phases except ice X (the larger excitation energy in ice X is due to the fact that it is a high pressure phase above ~150 GPa). Major spectral differences in these crystalline phases exist in the main peak area indicating this region is more sensitive to the local H-bond network. Therefore, this region offers the possibility to study the local environment of the absorbing oxygen atoms and this does not require long range order, as necessary in

X-ray diffraction (XRD). It has also been shown recently that similar agreements with XRD and neutron diffraction pattern are not distinguishable between some very different structure, especially in the H-bond systems[55,68-70] which also drives search for the new experimental tool to probe H-bond environments. Here, we showed that oxygen *K* edge XAS might be an effective structural tool to distinguish the similar H-bond systems.

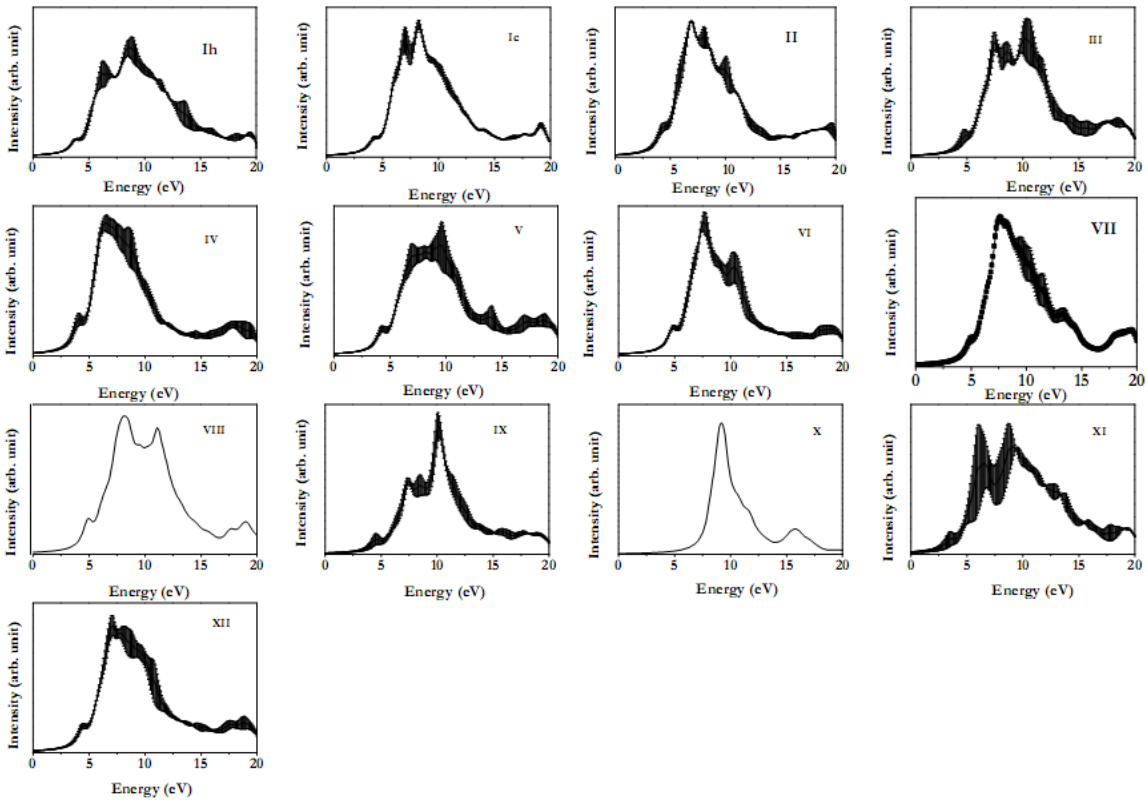

Fig. 4.5 Calculated oxygen *K* edge XAS with standard deviation in ice I_h, I_c, II, III, IV, V, VI VII, VIII, IX, X, XI, and XII.

In the following, we will analyze the origin of the spectral features in the oxygen *K* edge XAS and explain the disappearance of the pre-edge in ice X in terms of the oxygen *s-p* hybridization of the probed molecule. We should note here that in order to

compare with PDOS, oxygen *K* edge XAS in Fig. 4.6 was not shifted and the Fermi level was indicated as zero in the energy scale. We could see that the unbroadened DOS(*p*) of core-holes contributes mainly to oxygen *K* edge XAS, as expected from the dipole selection rule. Since molecular orbital $4a_1$ has strong *s* character, we used DOS(*s*) to locate the $4a_1$ energy range. In Fig. 4.6, it is obvious that DOS(*s*) has a very sharp peak at the pre-edge region in all these ice phases. Thus, we could deduce that the pre-edge mainly comes from oxygen $1s$-$4a_1$ transitions and the main peak has main contribution from oxygen $1s$-$2b_2$ transitions as there are little DOS(*s*)

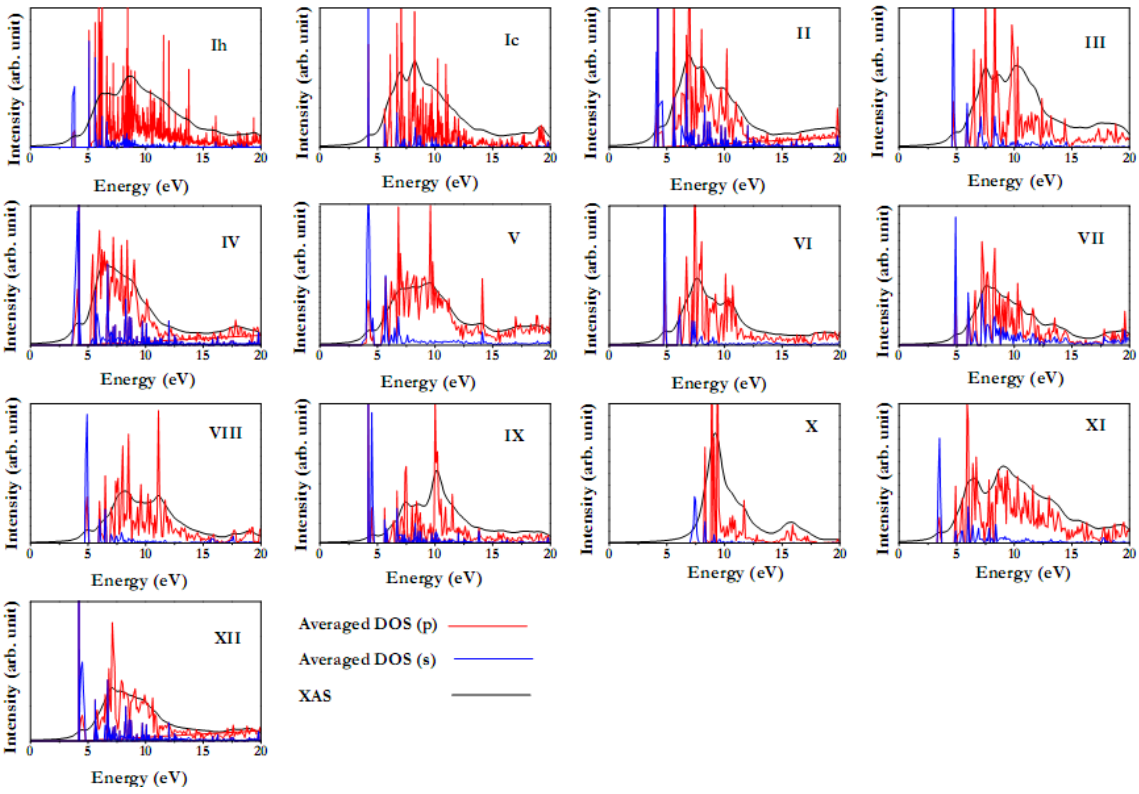

Fig. 4.6 Calculated oxygen *K* edge XAS (black solid lines) together with the unbroadened PDOS (*s* in blue line while *p* in red line).

contributions. In Fig. 4.5, the pre-edge (with the exception of ice X) locates around

3~5 eV with minor changes across different ice phases, but the main peaks show significantly different features in all these phases of the ice. Also, within a single phase the main peak has large standard deviation when different oxygen sites are excited.

4.3.3 Influence of pressure on the Oxygen *K* edge XAS in ice XIII

In the following, we will focus on this set of low-enthalpy structures in ice XIII given in Chap. 3 and investigate their absorption features in the oxygen *K* edge XAS at ambient pressure and high pressure with the purpose to provide helpful information on the local environments in these four structures. Oxygen *K* edge XAS spectra with standard deviation obtained by averaging over different oxygen sites are plotted in Fig. 4.7. The pre-edge feature (~535 eV) was observed in all these four structures and when selectively exciting different oxygen atoms with minor difference between these four configurations. However, we can see that the standard deviation is very large in the main peak region (536-542 eV), which reflects great sensitivity of this spectral region to the local chemical environment around oxygen atoms. Comparing these four configurations, the main spectra variances also lie in this main peak region. To summarize, this region offers the possibility to study the local environment of the absorbing oxygen atoms and does not require long range order, as necessary in XRD.

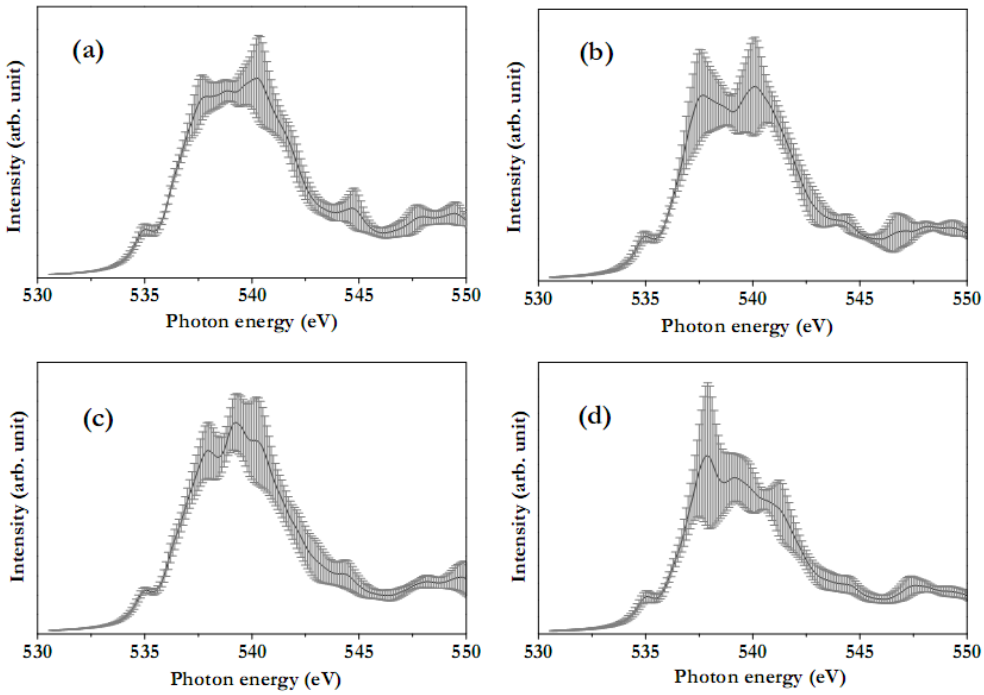

Fig. 4.7 (a)-(d) Calculated oxygen *K* edge XAS of the corresponding four structures given in Fig. 3.2 in Chap. 3 with standard deviation obtained by averaging over all distinct oxygen sites.

Furthermore, we probed effects of pressure on the oxygen *K* edge XAS. We carried out oxygen *K* edge XAS for structure (a) under 2 GPa as displayed in Fig. 4.8. Obviously, the oxygen *K* edge XAS shifts to higher energy by ~1 eV compared to 0 GPa. This could be understood as the increased band gap (~0.9 eV) under compression. We can see that the pressure suppresses the pre-edge intensity. When pressure is applied to ice, the covalent OH bond would become longer and the hydrogen bond became shorter[71,72]. This is consistent with the explanations in which weakened hydrogen bonds may enhance pre-edge intensity[7,8,73].

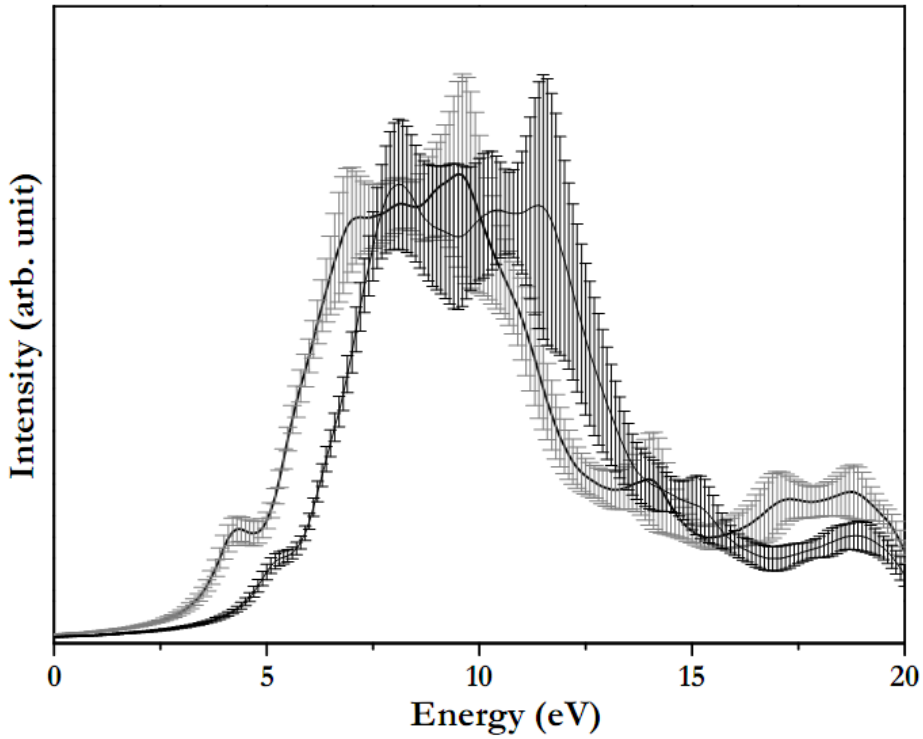

Fig. 4.8 Comparison of the calculated oxygen *K* edge XAS of structure (a) (shown in Fig. 3.2) under 0 GPa (grey) and 2 GPa (black).

The total electronic DOS and projected density of states (PDOS) of O-2*p* and H-1*s* calculated for structure (a) under pressure are shown in Fig. 4.9. PDOS provides information of the atoms, which influences the electronic states through variation in the angular momentum of the states. The DOS around the Fermi level comes mostly from O 2*p* and partially from 1s in H. We do not plot O-1*s* as it shows a very small effect on the total DOS in comparison with O-2*p*. The fully occupied sets of bands consist of the overlapping bands of both O-2*p* and H-1*s* states, indicating a strong bond between them. These bands are mainly responsible for the OH bond, exhibiting strong mixing. As for the total DOS, there is higher density at 0 GPa compared to higher pressure states near the Fermi level. The valence state of O can be

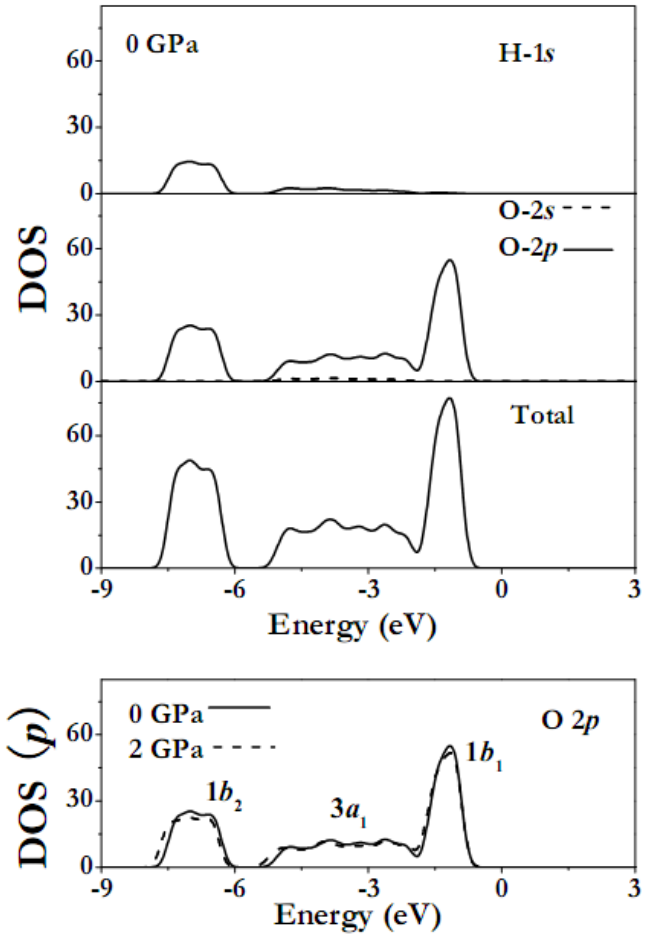

Fig. 4.9 Total DOS and PDOS for O 2*s*, O 2*p* electrons and H 1*s* electrons of structure a in different pressures (0 GPa, 2GPa).

evaluated from the distribution of O-2*p* electrons in the bonding $1b_2$+$3a_1$ bands We integrated the O-2*p* PDOS at 0 GPa, 2 GPa and the data are listed in Table 4.1, where $1b_2$+$3a_1$ denotes the energy from -8.16 to -1.81 eV and $1b_1$ shows the energy from -1.81 to -0.20 eV for the 0 GPa case.

Pressure	$3a_1+1b_2$	$1b_1$
0 GPa	62.06	39.01
2 GPa	61.23	40.12

Table 4.1 Integrated intensities of O-2*p* bands (electrons/unit cell) in structure (a) at different pressures.

As we can see from Table 4.1, the PDOS of the non-bonding $1b_1$ bands at 2 GPa is 1.11 element cells higher than that at 0 GPa, or the participation of 2*p* electrons in the 2*p*-1*s* hybridization at 2 GPa is less than those at 0 GPa. In other words, the covalent OH bond becomes weaker at high pressure, which is also evidenced by the increasing OH bond length (as discussed above) due to the increased attraction of the proton by the accepting oxygen ion[74]. This could also be interpreted as a general trend of OH bond in water system under compression, as verified through more ionic OH bond in the ice VII/VIII transition under pressure, and finally transformed into symmetric hydrogen bond phase ice X which is very similar to an ionic configuration[75].

4.3.4 Linkage between pre-edge to broken H-bond

To understand these observations, we examined orbital density difference between $2b_2$ and $4a_1$ [that is $\rho(2b_2)$-$\rho(4a_1)$] in one isolated water molecule with core hole effects as displayed in Fig. 4.10(d). It is known that the anti-bonding $4a_1$ orbitals in an isolated water molecule consist of O 3*s*-2*p* hybridized atomic orbitals extending

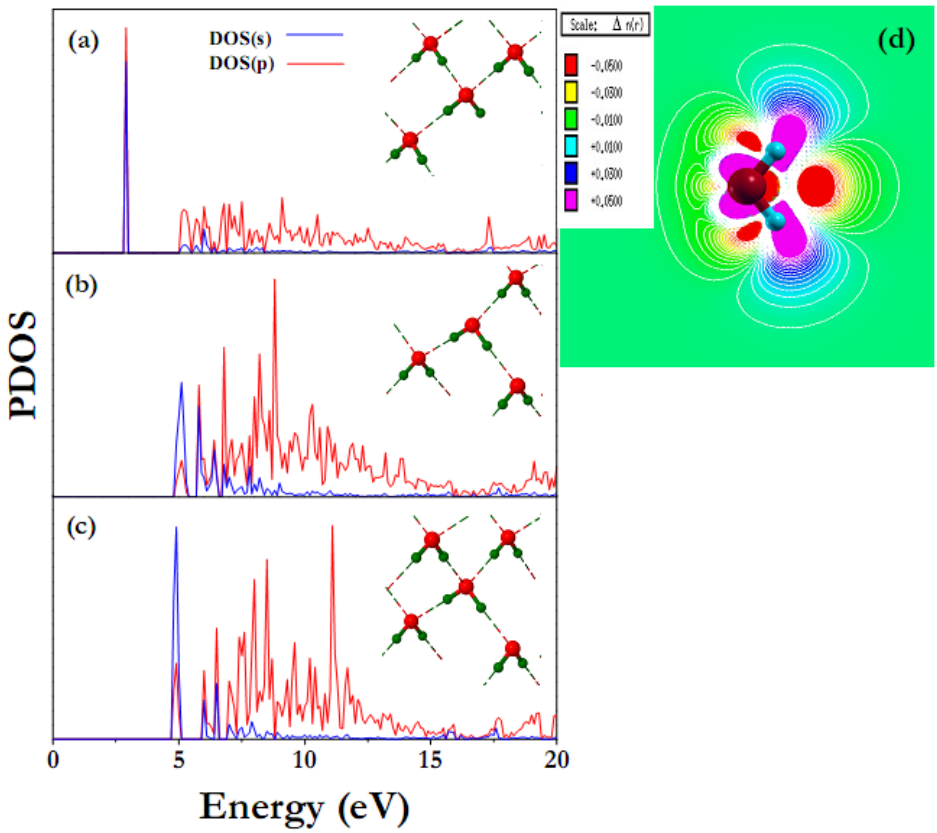

Fig. 4.10. Calculated projected density of states in ice VIII (*s* in blue line while *p* in red line) with schematic structure (red and green spheres representing oxygen and hydrogen atoms, respectively, dashed line representing H-bond) (a) remove one acceptor water molecule; (b) remove one donor water molecule (c) original ice VIII supercell lattice and (d) orbital density difference plot between $2b_2$ and $4a_1$ [$\rho(2b_2)$-$\rho(4a_1)$] in one isolated water molecule with core hole effects.

toward the c_2 axis, while two H 1*s* orbitals couple with each other through an in-phase manner. On the other side, the $2b_2$ orbitals are composed mainly of O 2*p* orbitals perpendicular to the c_2 axis and two H 1*s* orbitals through out-of-phase coupling. In Fig. 4.10(d), it can be observed that the positive regions of [$\rho(2b_2)$-$\rho(4a_1)$] are mainly along O-H bonds and around O with directions perpendicular to the c_2 axis. The negative regions, where $\rho(4a_1)$ is greater than $\rho(2b_2)$, resides mostly on the c_2 axis. Hence, the fact that $2b_2$ orbitals are more delocalized which is consistent with our

finding that the main peaks are more sensitive to the H-bond network in the vicinity of the excited oxygen. Moreover, out-of-phase coupling with H 1*s* orbitals in $2b_2$ orbitals includes more nodal planes compared with $4a_1$ orbitals, which enhances its electron kinetic energy and this implies that $2b_2$ orbitals could probe more out of H-bond network rather than $4a_1$ orbitals. Once again, we proved that main peak region shows great sensitivity to the local H-bond networks.

We all know that the structure symmetry would have a direct reflection in the molecular orbital mixing. In ice, the tetrahedral networks are pretty symmetric and this reduces the molecular orbital mixing. In contrast, the broken H-bonds destroy the symmetry and induce 3*s*-2*p* orbital hybridization. Hence, this explains why the pre-edge disappear in ice X since ice X is a very special ice phase with a perfect symmetric tetrahedral arrangement leaving the $4a_1$ level pure *s*-character. According to the dipole selection rule, there would be no transition in $4a_1$ level. Therefore, it is reasonable to link the pre-edge feature to broken H-bond.

Furthermore, an investigation of electronic structure change through deviating from tetrahedral symmetry in ice VIII by breaking H-bonds was carried out. We chose ice VIII here based on the fact that the structure of ice VIII is well-refined experimentally. The computed PDOS by removing one acceptor water molecule, one donor water molecule, and original ice VIII lattice, respectively, were shown in Fig. 4.10. It is obvious that the DOS(*s*) does not change much in these three configurations form Fig. 4.10(a) to Fig. 4.10(c). On the other side, breaking an accepting H-bond in Fig. 4.10(b) has very little effect on the DOS(*p*) while breaking a donating H-bond in Fig. 4.10(a),

however, is identified to bring a sharp DOS (*p*) at LUMO orbital with energy down-shifted ~2 eV compared to DOS (*p*) of original ice VIII lattice in Fig. 4.10(c). This down-shift behavior was also observed in the comparison of XAS between bulk ice I_h and ice I_h surface with broken H-bond presenting[7]. In the XAS study of methanol in linear chains and cyclic rings, Wilson *et al.* found the same pre-edge feature shifted higher in energy by ~1 eV for the molecules in the interior of chains or rings compared to the spectra of terminal molecules [76], and this shift has also been observed in the spectra of gas-phase methanol clusters[77]. An increase in the pre-edge intensity in oxygen *K* edge XAS was obviously emerged as displayed in Fig. 4.10(a). As discussed above, breaking the oxygen symmetry by deleting one water molecule from the hydrogen side (acceptor water molecule) brings in significant *p* character $4a_1$ orbitals and thus enhance the intensity of pre-edge in the oxygen *K* edge XAS. Similar conclusions were also drawn by previous works.[7,8,73] From this, one more time, we could also deduce that it is reasonable to link pre-edge with broken H-bond. There may be a question concerning why there is a huge difference appearing when removing an acceptor water molecule rather than a donor one. It is known that water molecule is highly polarized since the oxygen atoms has much higher electronegativity compared to hydrogen atoms. In the occupied orbitals, the polarizations points from H to O and in the unoccupied orbitals, it would be in opposite direction, towards to H. These unoccupied orbitals $4a_1$ and $2b_2$ would be more sensitive to the local changes in H sites than the O sites as reflected in the significant enhancement of the pre-edge in oxygen *K* edge XAS as shown in Fig.

4.10(c).

4.4 Conclusions

In conclusion, we have extensively and systematically studied the oxygen *K* edge XAS in most known crystalline phases of ice using DFT band structure calculation method. We achieved a very good agreement between the calculated and experimentally measured oxygen *K* edge XAS of ice I_h. More importantly, all ice phases show a universal pre-edge absorption around 535 eV in spite of the distinct local H-bond environments in different phases except ice X. From the analysis of the PDOS, we identified the origin of the spectral features in which transitions of oxygen 1*s*-4a_1 contribute mainly to the pre-edge while the oxygen 1*s*-2b_2 transitions give rise to the main peak in the oxygen *K* edge XAS. Major spectral differences exist in the main peak area indicating this region is very sensitive to the local H-bond network which offers an alternative structural tool to distinguish diverse H-bond structures. The disappearance of pre-edge in ice X is due to the perfect tetrahedral symmetry in ice X which makes 4a_1 level with pure *s* character. In other ice phases, the water molecules all have near-tetrahedral symmetry and this could reduce most of 4$a_1$orbitals's *p*-character, thus a very weak pre-edge appears. Further convincing proof is the significant enhancement of the pre-edge intensity in the oxygen *K* edge XAS when removing an acceptor water molecule. From this, we confirmed that the sensitivity of the pre-edge to the symmetry of oxygen atoms and the link between the pre-edge feature with broken H-bond is justified. This work was also expected to shed some light on the lately debate over the conventional tetrahedral H-bonded water or

chain-like water structure.

4.5 References

(1) Taylor, M. S.; Jacobsen, E. N. *Angewandte Chemie-International Edition* **2006**, *45*, 1520.

(2) Aakeroy, C. B.; Seddon, K. R. *Chemical Society Reviews* **1993**, *22*, 397.

(3) Cleland, W. W.; Frey, P. A.; Gerlt, J. A. *Journal of Biological Chemistry* **1998**, *273*, 25529.

(4) Ohmine, I.; Saito, S. *Accounts of Chemical Research* **1999**, *32*, 741.

(5) Steiner, T. *Angewandte Chemie-International Edition* **2002**, *41*, 48.

(6) Stohr, J. *Nexafs Spectroscopy* Springer-Verlag: New York, 1992.

(7) Wernet, P.; Nordlund, D.; Bergmann, U.; Cavalleri, M.; Odelius, M.; Ogasawara, H.; Naslund, L. A.; Hirsch, T. K.; Ojamae, L.; Glatzel, P.; Pettersson, L. G. M.; Nilsson, A. *Science* **2004**, *304*, 995.

(8) Myneni, S.; Luo, Y.; Naslund, L. A.; Cavalleri, M.; Ojamae, L.; Ogasawara, H.; Pelmenschikov, A.; Wernet, P.; Vaterlein, P.; Heske, C.; Hussain, Z.; Pettersson, L. G. M.; Nilsson, A. *Journal of Physics-Condensed Matter* **2002**, *14*, L213.

(9) Prendergast, D.; Galli, G. *Physical Review Letters* **2006**, *96*.

(10) Tse, J. S.; Shaw, D. M.; Klug, D. D.; Patchkovskii, S.; Vanko, G.; Monaco, G.; Krisch, M. *Physical Review Letters* **2008**, *100*.

(11) Mishima, O.; Stanley, H. E. *Nature* **1998**, *396*, 329.

(12) Nelmes, R. J.; Loveday, J. S.; Strassle, T.; Bull, C. L.; Guthrie, M.; Hamel, G.; Klotz, S. *Nat Phys* **2006**, *2*, 414.

(13) Tulk, C. A.; Benmore, C. J.; Urquidi, J.; Klug, D. D.; Neuefeind, J.; Tomberli, B.; Egelstaff, P. A. *Science* **2002**, *297*, 1320.

(14) Smith, J. D.; Cappa, C. D.; Wilson, K. R.; Messer, B. M.; Cohen, R. C.; Saykally, R. J. *Science* **2004**, *306*, 851.

(15) Wang, R. L. C.; Kreuzer, H. J.; Grunze, M. *Physical Chemistry Chemical Physics* **2006**, *8*, 4744.

(16) Hetenyi, B.; De Angelis, F.; Giannozzi, P.; Car, R. *Journal of Chemical*

Physics **2004**, *120*, 8632.

(17) Head-Gordon, T.; Johnson, M. E. *Proceedings of the National Academy of Sciences of the United States of America* **2006**, *103*, 7973.

(18) Nilsson, A.; Ogasawara, H.; Cavalleri, M.; Nordlund, D.; Nyberg, M.; Wernet, P.; Pettersson, L. G. M. *Journal of Chemical Physics* **2005**, *122*.

(19) Chen, W.; Wu, X. F.; Car, R. *Physical Review Letters*, *105*.

(20) Cai, Y. Q.; Mao, H. K.; Chow, P. C.; Tse, J. S.; Ma, Y.; Patchkovskii, S.; Shu, J. F.; Struzhkin, V.; Hemley, R. J.; Ishii, H.; Chen, C. C.; Jarrige, I.; Chen, C. T.; Shieh, S. R.; Huang, E. P.; Kao, C. C. *Physical Review Letters* **2005**, *94*, 025502.

(21) Pylkkanen, T.; Giordano, V. M.; Chervin, J. C.; Sakko, A.; Hakala, M.; Soininen, J. A.; Hamalainen, K.; Monaco, G.; Huotari, S. *Journal of Physical Chemistry B*, *114*, 3804.

(22) Fister, T. T.; Nagle, K. P.; Vila, F. D.; Seidler, G. T.; Hamner, C.; Cross, J. O.; Rehr, J. J. *Physical Review B* **2009**, *79*.

(23) Bergmann, U.; Wernet, P.; Glatzel, P.; Cavalleri, M.; Pettersson, L. G. M.; Nilsson, A.; Cramer, S. P. *Physical Review B* **2002**, *66*.

(24) Vinson, J.; Kas, J. J.; Vila, F. D.; Rehr, J. J.; Shirley, E. L. *Physical Review B*, *85*, 045101.

(25) Leetmaa, M.; Ljungberg, M. P.; Lyubartsev, A.; Nilsson, A.; Pettersson, L. G. M. *Journal of Electron Spectroscopy and Related Phenomena*, *177*, 135.

(26) Rehr, J. J.; Soininen, J. A.; Shirley, E. L. *Physica Scripta* **2005**, *T115*, 207.

(27) Laskowski, R.; Blaha, P. *Physical Review B*, *82*.

(28) http://www.lsbu.ac.uk/water/phase.html.

(29) Schwarz, K.; Blaha, P.; Madsen, G. K. H. *Computer Physics Communications* **2002**, *147*, 71.

(30) Hebert, C. *Micron* **2007**, *38*, 12.

(31) Titov, A.; Biquard, X.; Halley, D.; Kuroda, S.; Bellet-Amalric, E.; Mariette, H.; Cibert, J.; Merad, A. E.; Merad, G.; Kanoun, M. B.; Kulatov, E.; Uspenskii, Y. A. *Physical Review B* **2005**, *72*, 115209.

(32) Dong, C. L.; Persson, C.; Vayssieres, L.; Augustsson, A.; Schmitt, T.; Mattesini, M.; Ahuja, R.; Chang, C. L.; Guo, J. H. *Physical Review B* **2004**, *70*, 195325.

(33) Guo, J. H.; Vayssieres, L.; Persson, C.; Ahuja, R.; Johansson, B.; Nordgren, J. *Journal of Physics-Condensed Matter* **2002**, *14*, 6969.

(34) Perdew, J. P.; Burke, K.; Ernzerhof, M. *Physical Review Letters* **1996**, *77*, 3865.

(35) Monkhorst, H. J.; Pack, J. D. *Physical Review B* **1976**, *13*, 5188.

(36) Schwarz, K.; Wimmer, E. *Journal of Physics F-Metal Physics* **1980**, *10*, 1001.

(37) Schwarz, K.; Neckel, A.; Nordgren, J. *Journal of Physics F-Metal Physics* **1979**, *9*, 2509.

(38) Gao, S. P.; Pickard, C. J.; Payne, M. C.; Zhu, J.; Yuan, J. *Physical Review B* **2008**, *77*.

(39) Fortes, A. D.; Wood, I. G.; Brodholt, J. P.; Vocadlo, L. *Journal of Chemical Physics* **2003**, *119*, 4567.

(40) Salzmann, C. G.; Radaelli, P. G.; Hallbrucker, A.; Mayer, E.; Finney, J. L. *Science* **2006**, *311*, 1758.

(41) Kuhs, W. F.; Finney, J. L.; Vettier, C.; Bliss, D. V. *Acta Crystallographica Section A* **1984**, *40*, C114.

(42) Londono, J. D.; Kuhs, W. F.; Finney, J. L. *Journal of Chemical Physics* **1993**, *98*, 4878.

(43) Benoit, M.; Bernasconi, M.; Parrinello, M. *Physical Review Letters* **1996**, *76*, 2934.

(44) Leadbetter, A. J.; Ward, R. C.; Clark, J. W.; Tucker, P. A.; Matsuo, T.; Suga, H. *Journal of Chemical Physics* **1985**, *82*, 424.

(45) Zhang, J. Y.; Xiao, Z. R.; Kuo, J. L. *Journal of Chemical Physics*, *132*.

(46) Kuo, J. L.; Coe, J. V.; Singer, S. J.; Band, Y. B.; Ojamae, L. *Journal of Chemical Physics* **2001**, *114*, 2527.

(47) Kuo, J. L. *Physical Chemistry Chemical Physics* **2005**, *7*, 3733.

(48) Kuo, J. L.; Klein, M. L. *Journal of Physical Chemistry B* **2004**, *108*, 19634.

(49) Kuo, J. L.; Klein, M. L.; Kuhs, W. F. *Journal of Chemical Physics* **2005**, *123*.

(50) Kuo, J. L.; Kuhs, W. F. *Journal of Physical Chemistry B* **2006**, *110*, 3697.

(51) Kuo, J. L.; Singer, S. J. *Physical Review E* **2003**, *67*.

(52) Odelius, M. *Journal of Physical Chemistry A* **2009**, *113*, 8176.

(53) Wang, R. L. C.; Kreuzer, H. J.; Grunze, M. *Physical Chemistry Chemical Physics* **2006**, *8*, 4744.

(54) Cavalleri, M.; Odelius, M.; Nordlund, D.; Nilsson, A.; Pettersson, L. G. M. *Physical Chemistry Chemical Physics* **2005**, *7*, 2854.

(55) Iannuzzi, M. *Journal of Chemical Physics* **2008**, *128*, 204506.

(56) Rez, P.; Alvarez, J. R.; Pickard, C. *Ultramicroscopy* **1999**, *78*, 175.

(57) Triguero, L.; Pettersson, L. G. M.; Agren, H. *Physical Review B* **1998**, *58*, 8097.

(58) Buczko, R.; Duscher, G.; Pennycook, S. J.; Pantelides, S. T. *Physical Review Letters* **2000**, *85*, 2168.

(59) Tanaka, I.; Araki, H.; Yoshiya, M.; Mizoguchi, T.; Ogasawara, K.; Adachi, H. *Physical Review B* **1999**, *60*, 4944.

(60) Lie, K.; Hoier, R.; Brydson, R. *Physical Review B* **2000**, *61*, 1786.

(61) Elsasser, C.; Kostlmeier, S. *Ultramicroscopy* **2001**, *86*, 325.

(62) Hamann, D. R. *Physical Review B* **1997**, *55*, 10157.

(63) Umemoto, K.; Wentzcovitch, R. M.; Baroni, S.; de Gironcoli, S. *Physical Review Letters* **2004**, *92*.

(64) Klug, D. D.; Tse, J. S.; Liu, Z. X.; Gonze, X.; Hemley, R. J. *Physical Review B* **2004**, *70*.

(65) Rehr, J. J. *Radiation Physics and Chemistry* **2006**, *75*, 1547.

(66) Krisch, M.; Sette, F. "X-ray Raman scattering from low Z materials"; 13th International Conference on Vacuum Ultraviolet Radiation Physics (VUV-13), 2001, Trieste, Italy.

(67) Bergmann, U.; Glatzel, P.; Cramer, S. P. *Microchemical Journal* **2002**, *71*, 221.

(68) Soper, A. K. *Journal of Physics-Condensed Matter* **2005**, *17*, S3273.

(69) Leetmaa, M.; Wikfeldt, K. T.; Ljungberg, M. P.; Odelius, M.; Swenson, J.; Nilsson, A.; Pettersson, L. G. M. *The Journal of Chemical Physics* **2008**, *129*, 084502.

(70) Wikfeldt, K. T.; Leetmaa, M.; Ljungberg, M. P.; Nilsson, A.; Pettersson, L. G. M. *Journal of Physical Chemistry B* **2009**, *113*, 6246.

(71) Benoit, M.; Marx, D. *Chemphyschem* **2005**, *6*, 1738.

(72) Benoit, M.; Marx, D.; Parrinello, M. *Nature* **1998**, *392*, 258.

(73) Cavalleri, M.; Ogasawara, H.; Pettersson, L. G. M.; Nilsson, A. *Chemical Physics Letters* **2002**, *364*, 363.

(74) Vos, W. L.; Finger, L. W.; Hemley, R. J.; Mao, H. K. *Chemical Physics Letters* **1996**, *257*, 524.

(75) Caracas, R. *Physical Review Letters* **2008**, *101*.

(76) Wilson, K. R.; Cavalleri, M.; Rude, B. S.; Schaller, R. D.; Catalano, T.; Nilsson, A.; Saykally, R. J.; Pettersson, L. G. M. *Journal of Physical Chemistry B* **2005**, *109*, 10194.

(77) Tamenori, Y.; Okada, K.; Takahashi, O.; Arakawa, S.; Tabayashi, K.; Hiraya, A.; Gejo, T.; Honma, K. *Journal of Chemical Physics* **2008**, *128*.

Chapter 5

In this chapter, we presented our study on the structural and vibrational properties of filled ice C_2 hydrogen hydrate under compression by first principles molecular dynamics (FPMD). We found tetragonal symmetry of hydrogen hydrate ($P4_12_12$ and $Pna2_1$ space group) in our FPMD at low temperature. This finding demonstrates that the thermal effects play an essential role in stabilizing the structure to appear as cubic below 40 GPa. We also observed an indication of transition to an unknown high pressure phase above 40 GPa which is consistent with the experimental findings. Moreover, we determined the phase boundary line between hydrogen bond ordered (disordered) phases and the H_2 rotation and non-rotation phases at a rough approximation which may provide hints for further experiments. Hydrogen bond is predicted to symmetrize below 60 GPa based on the analysis of O-H stretching frequencies and radial distribution function g(OH). In comparison with the pure ice VII, the hydrogen bond symmetrization pressure in C_2 hydrogen hydrate is much lower, being reduced by a factor of two.

First principles molecular dynamics study on filled ice hydrogen hydrate under pressure

5.1Introduction

Alternative energy resources were widely explored since the limited capacity of the

fossil energy and its related environmental problems. Hydrates of natural gases suchas CH_4-H_2O[1-3] prevails in deep-sea sediments and permafrost have received active attention and been proposed as one of these energy resources[4]. More recently, hydrogen hydrate receives intensive attention since it facilitates environmentally clean (water is the only by-product) and highly efficient energy conversion. From an astronomical point of view, water exists largely on the giant planets, like Uranus and Neptune.[5-8] Extrasolar planets may have the possibility to contain large amount of water.[9,10] On the other side, hydrogen is the richest element in the whole universe.[11] Above 0.8 GPa and room temperature, water and hydrogen would be synthesized into hydrogen hydrate. Therefore, study of hydrogen hydrate under pressure has wide implications in astrophysics.

At present, three forms of hydrogen hydrates exist under different conditions. The first one is a clathrate hydrate, sII structure which was synthesized by compressing a mixture of H_2 and H_2O to pressures of 180 to 220 MPa at 300 K,[12,13] [14,15] [16]and another two are filled-ice phases, C_1 and C_2, which were synthesized above 0.8 and 2.4 GPa at room temperature, respectively..[17-20] The filled ice hydrate C_2 is composed of a host ice Ic structure while the hydrogen molecules located in the interstitials of ice Ic[17] (as shown in Fig. 5.1). Pressure-induced phase transitions were investigated using x-ray diffraction (XRD) and Raman spectroscopy.[19,20] In the low pressure region, C_2 hydrogen hydrate remains a cubic crystal structure and structural transitions were observed around 35-40 and 55-60 GPa and the high-pressure phase can survive up to

80.3 GPa.[20] However, these two high-pressure phases have not been determined experimentally.

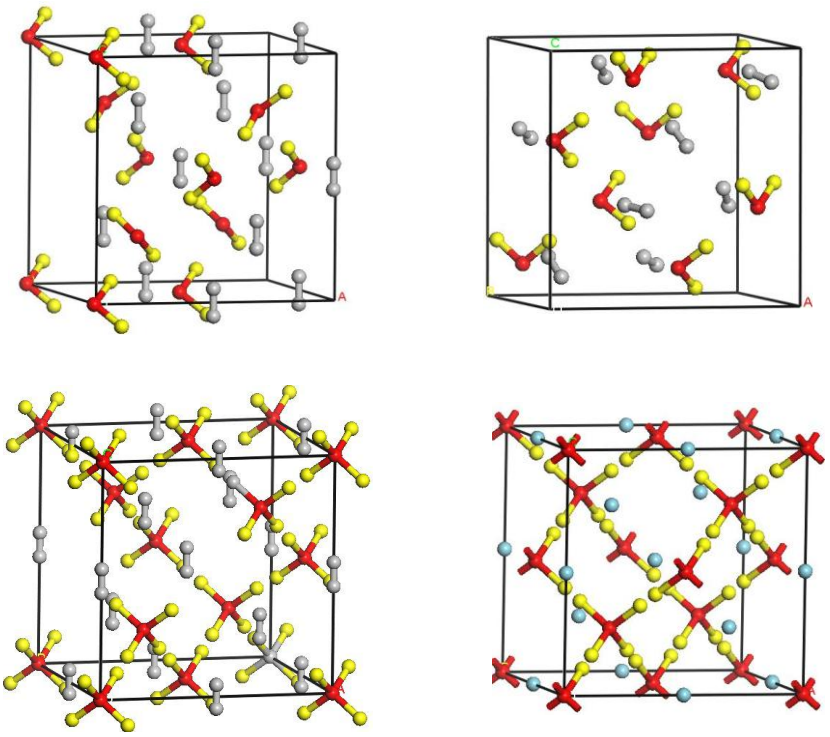

Fig. 5.1 (Color online) Four schematic models of structure. (a) space group $P4_12_12$; (b) space group $Pna2_1$; (c) space group $I4_1/amd$. H atoms of H_2O have half occupation indicating the hydrogen bond disordered network; (d) space group Fd-3m. H atoms of H_2O have half occupation. The rotating guest H_2 molecules are represented by a light blue sphere; The red balls represent oxygen atoms in water molecules, the yellow balls indicate hydrogen atoms in water molecules, the grey balls indicate the hydrogen atoms of the hydrogen molecules.

There are enormous investigations on proton ordering transitions in ice, like ice I*h*/XI[21-26], V/XIII, VI/XV, VII/VIII[27-31], XII/XIV transitions. Similarly, we would also like to study the proton ordering in the H_2-H_2O at low temperature. With the aim to roughly estimate the phase diagram to see the influence of pressure and temperature, we constructed four hydrogen bond ordered (disordered) phases and H_2 rotation (non-rotation) phases and then attempted to determine the phase boundary lines.

As we all know, vibrational spectroscopy is a very widely-used in structural characterization. To analyze the spectra, it would be helpful to understand the atomic vibration movement in microscopic level. Therefore, it is better to have theoretical comparison and support. The hydrogen molecules vibron could provide information on the interaction between guest hydrogen molecules and the host water molecules and also may influence the hydrate stabilities. Up to now, to our best knowledge, there is little theoretical report carried out on C_2 hydrogen hydrate under high pressure. Therefore, further theoretical studies were motivated in structural and vibrational properties under compression.

5.2 Computation methods

First-principle molecular dynamics (MD) simulations at finite temperature and geometry optimization at 0 K were carried out by means of density functional theory (DFT) calculations using a pseudopotential plane wave approach implemented in the Quantum-Espresso Package [32-34] with ultrasoft pseudopotential using the BLYP functional [35]. We adopted NPT ensemble here to study the pressure and temperature effects. These simulations are investigated with 8 water molecules and 8 hydrogen molecules at a constant temperature of 300 K with pressure range from 3 GPa to 100 GPa. The simulations ran around at least 15 ps which is enough for all the pressure points with time step of 0.5 fs. We used a plane wave cutoff energy of 35 Ry and a $2\times2\times2$ Monkhorst-Pack (MP) grid (*k*-mesh) for the electronic Brillouizone integration.

A more strict condition with cutoff energy up to 100 Ry and 9×9×6 MP grid was employed in the phonon calculation using the linear-response method.[36] In this work, we also calculated the vibrational frequencies from the Fourier transformation of the velocity auto-correlation function obtained from the MD trajectories. This method takes anharmonic effects into account. We have broadened the theoretical spectra with a Lorentzian of full width at half maximum FWHM = 30 cm^{-1}.

5.3Results and Discussions

5.3.1 Zero temperature results

Here, we employed all possible ice-rule-allowed configurations enumeration scheme[37,38] to construct the host ice lattice, i.e. ice Ic, which have been successfully applied to ice Ih[39], ice VII/VIII[40,41], and ice VI[42] in our previous works. Analyzing the symmetry of the all the configurations in the cubic ice Ic, there are four class of space groups: P43, $P4_12_12$, $Pna2_1$ and $I4_1md$. Then, we continue to build the H_2-H_2O structure by putting H_2 in the Ic lattice interstitial sites. We followed two ways to add H_2 of different orientations, one is all parallel to each other and the other is orientationally disordered. Therefore, we have constructed 8 H_2-H_2O possible structures.

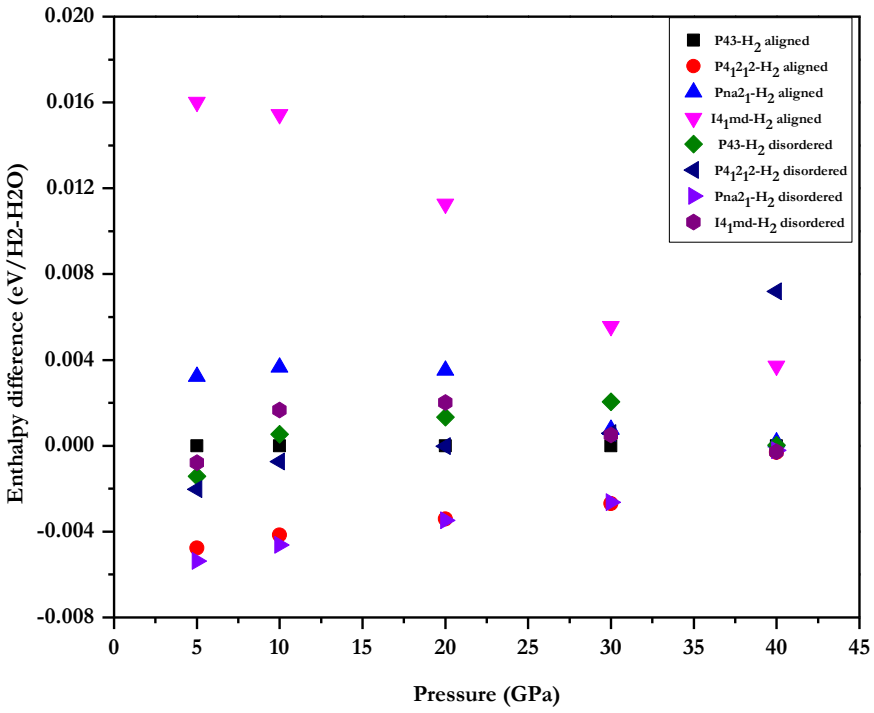

Fig. 5.2 (Color online) Relative enthalpies of 8 H_2-H_2O candidate structures described in the text as a function of pressure.

Full geometry optimizations were carried out for all the structures from 5-40 GPa and the relative stability was shown in Fig. 5.2 From the figure, we could see that arrangements of H_2 affect the stability and two structures ($P4_12_12$-H_2 aligned and $Pna2_1$-H_2 disordered) are comparatively energetic favorable. Therefore, these two structures are the possible candidate structures of H_2-H_2O at 0 K from the thermodynamic criteria. Furthermore, dynamical stability calculation of phonon dispersion was carried out by DFT linear-response theory from 3 GPa to 60 GPa and all the frequencies were positive at these pressures showing the structure is dynamically stable at 0 K. It is essential to be note that the previous reported cubic Fd-3m space group[17] corresponds to the the symmetry of oxygen lattice only. In this

sense, the experimental reported "*cubic*" term refers to the oxygen lattice symmetry. Thus including the hydrogen atoms of water molecules and guest hydrogen molecules would change the symmetry and this also explains why we could observe the tetragonal symmetry at low temperature as discussed above. However, we still stick to this conventional '*cubic*' term in the following discussions for consistency. The calculated equation of state (EOS) of structure $P4_12_12$-H_2 aligned is compared with the experimental data[20] as shown in Fig 5.3 The EOS of 0 K shows a very similar trend with experimental data while the volume values are within 6% smaller below 30 GPa.

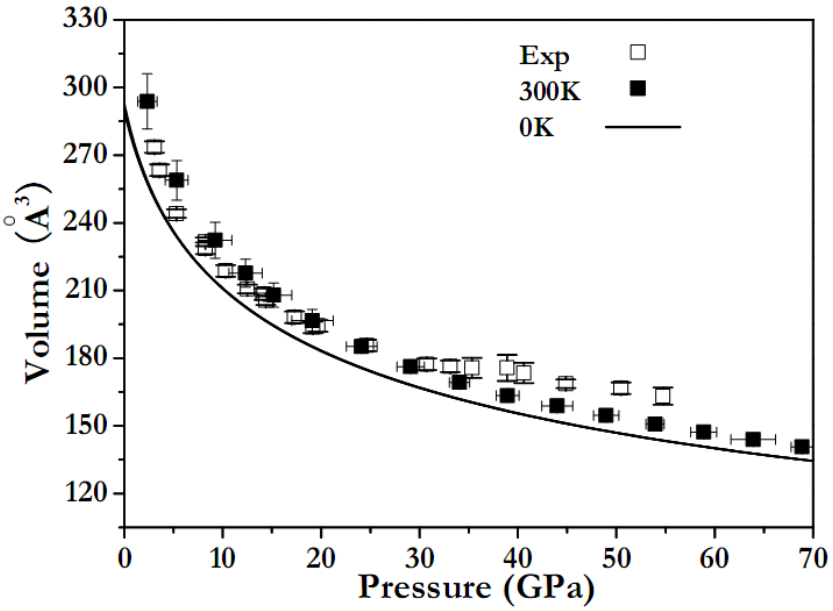

Fig. 5.3 Comparison of calculated equation of states at 0 K and 300 K of structure $P4_12_12$-H_2 aligned (solid line and solid squares with error bar, respectively) with experimental data in Ref. 25 (open squares with error bar).

5.3.2 Finite temperature effects (300 K)

For simplicity, we adopted the structure $P4_12_12$-H_2 aligned as our initial structure for MD runs which shows energetic competitive in low temperature. At room temperature, the equilibrium structure in low pressure (< 30 GPa) is '*cubic*' of which the water sublattice remains the $P4_12_12$ space group symmetry while H_2 molecules fastly rotate and vibrate. The agreement between theoretical EOS at 300 K and the experimental data is very good below 30 GPa (Fig. 5.3), lending support in the validity theoretical model employed here. This finding demonstrates that the thermal effects play an essential role in stabilizing the structure to appear as cubic below 40 GPa, hence, highlights the importance of taking temperature into account to study this system. The discrepancy above 30 GPa might be attributed to the fact that experimental volume value was calculated assuming the structure remains '*cubic*' symmetry and this is problematic and may cause error. In fact, there are pressure induced phase transitions as evidenced by new diffraction line resulting from the splitting of (220) around 40.5 GPa[20] and in another study[18], the same splitting was also reported around 30-35 GPa.

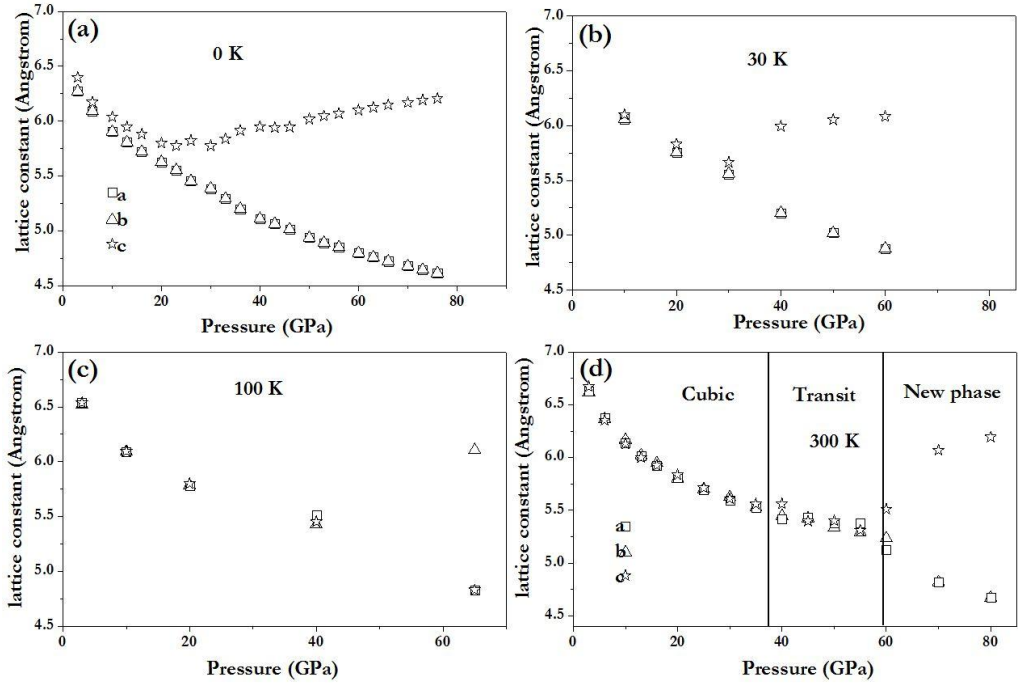

Fig. 5.4 Lattice constant evolution at 0K , 30K, 100K, and 300 K as a function of pressure in which *a*, *b*, *c* was indicated as empty squares, triangles, and stars, respectively.

The evolution of cell size (lattice constant *a*, *b*, and *c*) under pressure and finite temperature (0K, 30 K, 100 K, 300 K) in MD simulation was investigated in Fig. 5.4(b)-(d). There is a obvious trend that the temperature stabilizes the '*cubic*' structure from Fig. 5.4 (b) to Fig. 5.4 (d). It is easy to see that the structure appears as '*cubic*' (*a* = *b* = *c*) below 35 GPa and transit into (*a* = *b*< *c*) structure which confirms the experimental structural change findings as illustrated in Fig. 5.4(d). Again, this emphasized the essential role of the temperature in stabilizing the H_2-H_2O as 'cubic'. The transition starts around 40 GPa evidencing by non-identical lattice constants and completely finish around 60 GPa. We double-checked this phenomenon with a larger cell MD run with 16 H_2O molecules and 16 H_2 and the conclusion remained valid.

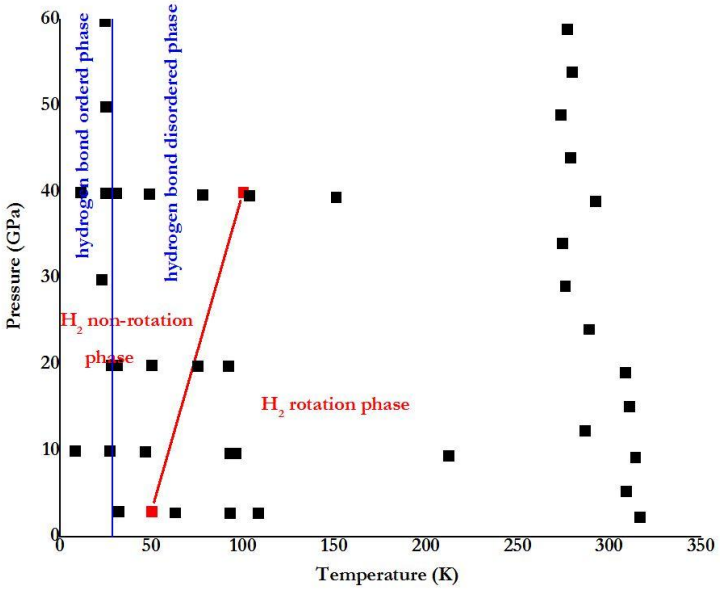

Fig. 5.5 Phase diagram of H_2-H_2O's four possible states and all the (P,T) conditions in our MD simulation shown in solid squares.

And then, we took one more step towards mapping the phase diagram of H_2-H_2O as illustrated in Fig. 5.5. Considering the hydrogen bond network orderd (disordered) or the H_2 rotation (non-rotation) in the influence of temperature, there are going to be four combinations. For the phase boundary between the H_2 rotation phase and non-rotation phase, we carried out MD at different temperatures and different pressure and all the simulated (P,T) points are listed in Fig. 5.5. From the MD trajectory movie, we determine this phase boundary line from 3-40 GPa (red line in Fig. 5.5). It is well known that Pauling[43] deduced the residual configurational entropy of a completely hydrogen disordered phase to be $k_b\ln(3/2)$ from a pure theoretical estimation, that is 3.37 J/mol/K, in remarkably agreement with the later experiment on ice I_h.[44] According to the third law of thermodynamics, there is no configuration entropy of a

hydrogen ordered phase of ice. Therefore, we could take the Pauling entropy to estimate the transition from complete hydrogen order to complete hydrogen disorder. Then considering the formula $\Delta G=TS=k_bTln(3/2)$[45], the transition temperature from hydrogen bond ordered-disordered transition lies around 29 K which is similar to the ice I_h-XI transition (around 72 K).[46] Since the configuration entropy does not depend on the pressure, this phase boundary line is parallel to the pressure axis. From the experimental point view, neutron diffraction measurements might be the effective tool to determine the hydrogen bond ordered phase of H_2-H_2O which showed great success in the ice system, i.e. ice VIII[28,31,47], ice XI[22,24,46,48], ice XIII and ice XIV[49], ice XV[50]. There are several possible methods for determining the boundary between the hydrogen rotating phase and non-rotating phase. Inelastic neutron scattering was used to study the rotation of guest molecules in methane hydrate[51]. Quasielastic neutron scattering was used to investigate the hydrogen dynamics in crystalline calcium borohydride such as rotations, librations, and vibrations[52]. Proton NMR[53-56] and Raman spectroscopy[19,20] can detect the rotation of H_2 molecules in clathrates. In particular, the diamond anvil cell NMR [56] revealed the molecular rotation and diffusion of H_2 molecules in the filled-ice hydrogen hydrate at pressures up to 3.6 GPa.

We calculated the vibratioanl frequency from the MD trajectory, so called velocity autocorrelation method[57-59]. PDOS together with O-H vibration frequencies calculated from linear-response theory, and experimental vibron frequency[20] under compression were displayed in Fig. 5.6.

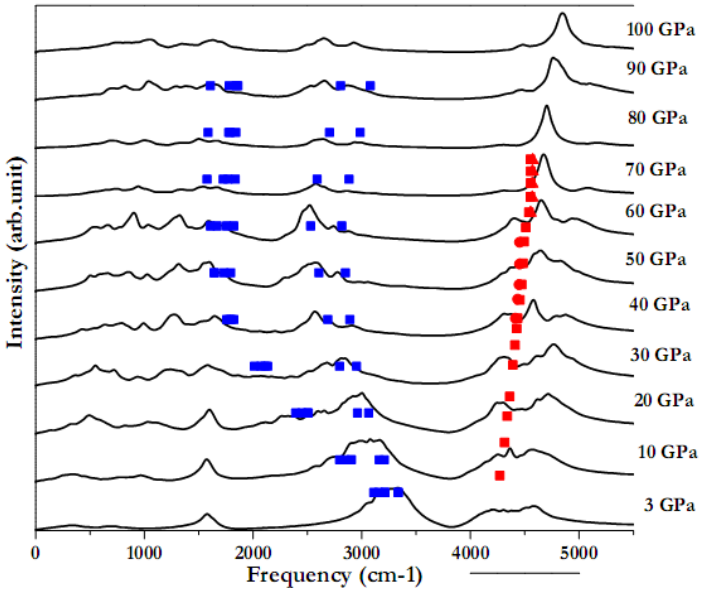

Fig. 5.6 (Color online) Comparison of simulated phonon density of states (solid line) from MD trajectory with the frequency (solid blue squares) calculated with linear response theory and the experimental data in Ref. 25 (red symbols).

There is a good agreement in frequency peak positions between experimental vibron frequency with the calculated PDOS. The blue-shift of the vibron frequency is consistent with the pure H_2 behavior under pressure. The O-H vibration frequencies calculated from linear-response theory also match well with the PDOS obtained from MD trajectories and separate into two groups. This separation behavior of the stretching mode is also observed in the O-H vibrations of HDO molecules in D_2O.[60,61] Meanwhile, O-H vibration frequency decreases and then increases when increasing

pressure. Red-shift of O-H vibration frequency under compression is a common feature in water system, corresponding to that O-H bond strength becomes weaker and its bond length becomes longer due to the increased attraction of the proton by the accepting oxygen. This also facilitates H-bond symmetrization as discussed below.

5.3.3 H-bond symmetrization

H-bond symmetrization in ice is a result of the proton motions and has been studied over a half century.[62-65] The energy potential felt by the proton motion between its neighboring two oxygen atoms has double minima. When applying pressure, the potential barrier at the midpoint of two O-O will be lowered until it disappears, hence, single well potential forms. At first, the hydrogen occupied asymmetric positions between two oxygen atoms will move to the midpoints. This process involves the proton displacement, and hence, it is similar to the displacive-type phase transitions which were induced by soft-mode in certain vibration modes. In Fig. 5.6, the calculated O-H stretching vibration in C_2 hydrogen hydrate (blue squares) softens as a function of pressure and hardens above around 60 GPa. We deduced that the H-bond symmetrized below 60 GPa, the intersection point, which is much larger than the experimental value of 40 GPa[18,20].

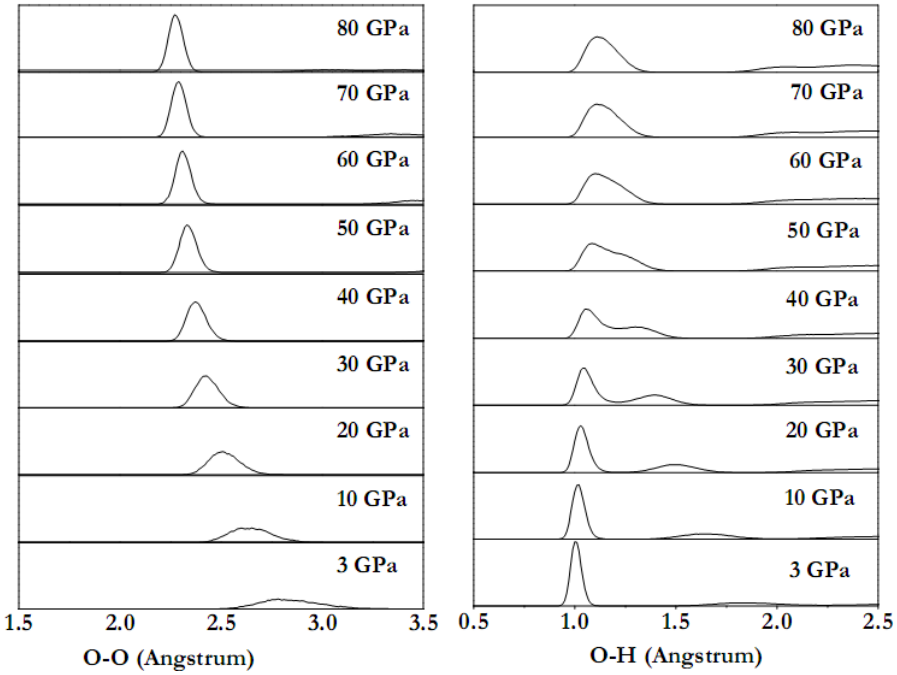

Fig. 5.7 Radial distribution function g(OO) and g(OH) as a function of pressure of hydrogen hydrate at 300K.

The structure changes are shown in Fig. 5.7 through the atomic radial distribution function under pressure. The effect of pressure is to shorten O-O distance and to lengthen the O-H bond length. We could see the O-O distance shorten under pressure as shown in g(OO) plot in Fig. 5.7. The first peak position (~ 1 Å) in g(OH) is the covalent O-H bond length and the second peak denotes the O.....H H-bond length while the broad band afterwards represents distance from oxygen to the guest H_2 molecules. The second peak was observed to move near to first peak and incorporate together around 60 GPa, indicating the hydrogen atoms locate in the middle point between two neighboring oxygen atoms. Therefore, the same conclusion could also be drawn from the radial distribution function g(OH). To further investigate the thermal

hopping behavior of the hydrogen atoms, we plotted the probability distribution of hydrogen atom along a hydrogen bond at room temperature. Benoit *el al*[66] came up with a three stage scenario theory to illustrate the H-bond symmetrization in ice with increasing pressure in which under low pressure the ice is a molecular state with normal H-bond, then under medium pressure hydrogen atoms begins to move back and forth in two potential minima (deep tunneling region or ionization), finally under certain pressure hydrogen atoms locate exactly at the midpoint between two neighboring oxygen atoms, symmetrization happens. From Fig. 5.8, the probability distribution of d(OH)/d(OO) clearly follows the three-stage scenario in hydrogen hydrate as it was shown for methane hydrate[1].

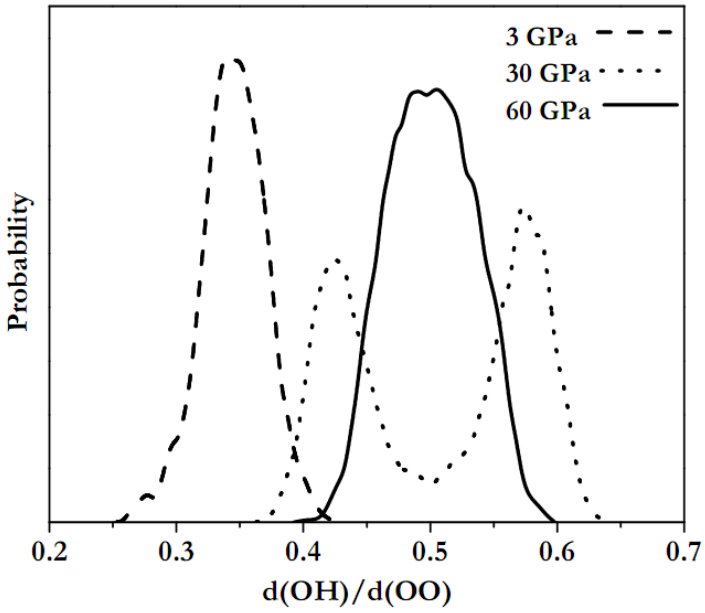

Fig. 5.8 Distribution of hydrogen atom along a hydrogen bond of C_2 hydrogen hydrate at 300 K and 3, 30, 60 GPa, respectively.

Moreover, we would like to comment on the relation in H-bond symmetrization between C_2 hydrogen hydrate and ice VII. The calculated O-O distance and the ratio

of d(OH)/d(OO) in C_2 hydrogen hydrate together with experimental data and in ice VII at 0 K were shown in Fig. 5.9. The calculated O-O distance in Fig. 5.9(a) coincides well with experimental results below 30 GPa while large difference was observed in high pressure region. A possible explanation would be the experimental results were obtained by assuming '*cubic*' symmetry in all the pressure range and calculating the O-O distance directly by the lattice parameter *a* as: $d_{O-O}=\frac{1}{4}\sqrt{3}a$ and this would cause error as also in the EOS. The predicted distances between two neighboring oxygen atoms (d_{O-O}) of 2.44, 2.36, and 2.27 Å are the onset of proton tunneling and unimodal distribution, and single well potential[66,67] as indicated by horizontal bars in Fig. 5.9(a) and Fig. 5.9(b). We could see that the H-bond symmetrization (dOH/dOO = 0.5) took place around 50 GPa and 120 GPa for C_2 hydrogen hydrate and ice VII, respectively, deduced from Fig 5.9(c) and Fig. 5.9(d). In comparison with d_{O-O} calculations in ice VII, we found that the pressure dependence of d_{O-O} is significantly larger than ice VII and this dependence could be mapped onto that of ice VII by doubling the pressure which was also indicated in an experimental report[18]. From this point of view, the properties of C_2 hydrogen hydrate at a given pressure are a good model for H_2O at approximately twice that pressure.

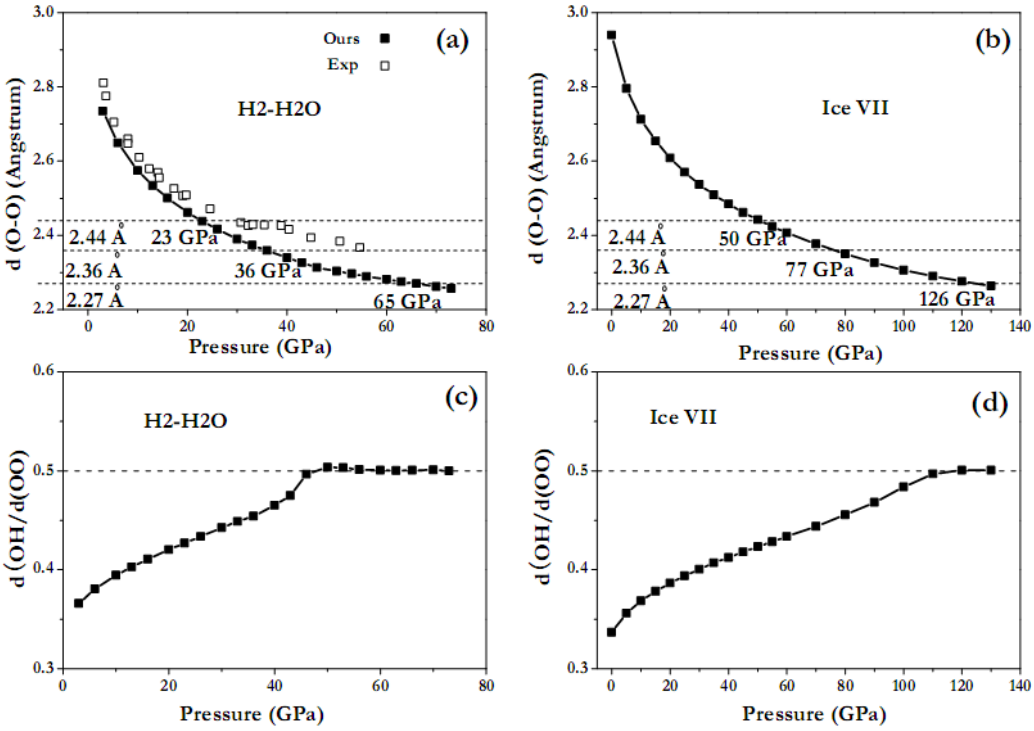

Fig. 5.9 Calculated oxygen oxygen distance and the ratio d(OH)/d(OO) in C_2 hydrogen hydrate and ice VII at 0 K.

5.4 Summary

In this work, structural changes, phase diagram, and vibrational properties were investigated using first principles MD. Experimentally reported '*cubic*' structure was found not stable in the zero temperature simulation. This is understandable since experimentally reported cubic Fd-3m (space group) C_2 phase reflects the symmetry at high (room) temperature when the hydrogen bond network is disordered and the hydrogen molecules are orientationally disordered. In this sense, the '*cubic'* symmetry would definitely be lowered at low temperature where the hydrogen bond network is ordered and the hydrogen molecules are aligned. Actually, two structures $P4_12_12$-H_2

aligned and $Pna2_1$-H_2 disordered are found to be energetically competitive at 0 K and 5-40 GPa. At room temperature, it is the thermal effects that play an essential role in stabilizing the structure in '*cubic'* symmetry below 30 GPa. We also observed a phase transition to an unknown new phase around 40 GPa at room temperature which gains agreement with the experimental finding. Furthermore, phase diagram of four phases (hydrogen bond ordered-disorderd, H_2 rototaion-nonrotation) was estimated at a first approximation which could provide hints for further experiments. PDOS was extracted from Fourier analysis of the MD trajectories, which are in good agreement in the peak positions with experimental data. H-bond symmetrization was inferred to happen below 60 GPa from analysis of soft mode O-H vibrational frequency and radial distribution of g(OH) under compression. In comparison with the pure ice VII, the hydrogen bond symmetrization pressure in C_2 hydrogen hydrate is much lower, being reduced by a factor of two.

5.5References:

(1) Iitaka, T.; Ebisuzaki, T. *Physical Review B* **2003**, *68*, 4.

(2) Loveday, J. S.; Nelmes, R. J.; Guthrie, M.; Belmonte, S. A.; Allan, D. R.; Klug, D. D.; Tse, J. S.; Handa, Y. P. *Nature* **2001**, *410*, 661.

(3) Loveday, J. S.; Nelmes, R. J.; Guthrie, M.; Klug, D. D.; Tse, J. S. *Physical Review Letters* **2001**, *87*, 4.

(4) Sloan, E. D. *Clathrate Hydrates of Natural Gases*; Marcel Dekker: New York, 1990.

(5) *Physics of Planetrary Interiors*; Zharkov, V. N.; P., T. V., Eds.; Parchart: Tucson, 1978.

(6) Hubbard, W. B. *Science* **1981**, *214*, 145.

(7) Pollack, J. B.; Hubickyj, O.; Bodenheimer, P.; Lissauer, J. J.; Podolak, M.; Greenzweig, Y. *Icarus* **1996**, *124*, 62.

(8) Guillot, T. *Science* **1999**, *286*, 72.

(9) Baraffe, I.; Chabrier, G.; Barman, T. *Astronomy & Astrophysics* **2008**, *482*, 315.

(10) Guillot, T. *Annual Review of Earth and Planetary Sciences* **2005**, *33*, 493.

(11) http://en.wikipedia.org/wiki/Hydrogen.

(12) Mao, W. L.; Mao, H. K.; Goncharov, A. F.; Struzhkin, V. V.; Guo, Q. Z.; Hu, J. Z.; Shu, J. F.; Hemley, R. J.; Somayazulu, M.; Zhao, Y. S. *Science* **2002**, *297*, 2247.

(13) Lokshin, K. A.; Zhao, Y. S.; He, D. W.; Mao, W. L.; Mao, H. K.; Hemley, R. J.; Lobanov, M. V.; Greenblatt, M. *Physical Review Letters* **2004**, *93*, 4.

(14) Mao, W. L.; Mao, H. K. *Proceedings of the National Academy of Sciences of the United States of America* **2004**, *101*, 708.

(15) Patchkovskii, S.; Tse, J. S. *Proceedings of the National Academy of Sciences of the United States of America* **2003**, *100*, 14645.

(16) Strobel, T. A.; Sloan, E. D.; Koh, C. A. *Journal of Chemical Physics* **2009**, *130*.

(17) Vos, W. L.; Finger, L. W.; Hemley, R. J.; Mao, H. K. *Physical Review Letters* **1993**, *71*, 3150.

(18) Vos, W. L.; Finger, L. W.; Hemley, R. J.; Mao, H. K. *Chemical Physics Letters* **1996**, *257*, 524.

(19) Hirai, H.; Ohno, S.; Kawamura, T.; Yamamoto, Y.; Yagi, T. *Journal of Physical Chemistry C* **2007**, *111*, 312.

(20) Machida, S.; Hirai, H.; Kawamura, T.; Yamamoto, Y.; Yagi, T. *Journal of Chemical Physics* **2008**, *129*.

(21) Tajima, Y.; Matsuo, T.; Suga, H. *Nature* **1982**, *299*, 810.

(22) Jackson, S. M.; Nield, V. M.; Whitworth, R. W.; Oguro, M.; Wilson, C. C. *The Journal of Physical Chemistry B* **1997**, *101*, 6142.

(23) Jackson, S. M.; Whitworth, R. W. *The Journal of Physical Chemistry B* **1997**, *101*, 6177.

(24) Line, C. *J. Chem. Phys.* **1996**, *104*, 10008.

(25) Jackson, S. *J. Chem. Phys.* **1995**, *103*, 7647.

(26) Kuo, J. *J. Chem. Phys.* **2005**, *123*, 134505.

(27) Johari, G. *J. Chem. Phys.* **1974**, *61*, 4292.

(28) Kuhs, W. *J. Chem. Phys.* **1984**, *81*, 3612.

(29) Singer, S. J.; Kuo, J.-L.; Hirsch, T. K.; Knight, C.; Ojamae, L.; Klein, M. L. *Physical Review Letters* **2005**, *94*, 135701.

(30) Kuo, J.-L.; Klein, M. L. *The Journal of Physical Chemistry B* **2004**, *108*, 19634.

(31) Jorgensen, J. *J. Chem. Phys.* **1984**, *81*, 3211.

(32) Scandolo, S.; Giannozzi, P.; Cavazzoni, C.; de Gironcoli, S.; Pasquarello, A.; Baroni, S. *Zeitschrift Fur Kristallographie* **2005**, *220*, 574.

(33) Giannozzi, P.; Baroni, S.; Bonini, N.; Calandra, M.; Car, R.; Cavazzoni, C.; Ceresoli, D.; Chiarotti, G. L.; Cococcioni, M.; Dabo, I.; Corso, A. D.; Gironcoli, S. d.; Fabris, S.; Fratesi, G.; Gebauer, R.; Gerstmann, U.; Gougoussis, C.; Kokalj, A.; Lazzeri, M.; Martin-Samos, L.; Marzari, N.; Mauri, F.; Mazzarello, R.; Paolini, S.; Pasquarello, A.; Paulatto, L.; Sbraccia, C.; Scandolo, S.; Sclauzero, G.; Seitsonen, A. P.; Smogunov, A.; Umari, P.; Wentzcovitch, R. M. *Journal of Physics: Condensed Matter* **2009**, *21*, 395502.

(34) S. Baroni, A. D. C., S. de Gironcoli, and P. Giannozzi, C. Cavazzoni, G. Ballabio, S. Scandolo, G. Chiarotti, P. Focher, A. Pasquarello, K. Laasonen, A. Trave, R. Car, N. Marzari, and A. Kokalj. http://www.quantum-espresso.org/.

(35) Becke, A. D. *Physical Review A* **1988**, *38*, 3098.

(36) Giannozzi, P.; de Gironcoli, S.; Pavone, P.; Baroni, S. *Physical Review B* **1991**, *43*, 7231.

(37) Knight, C.; Singer, S. J.; Kuo, J.-L.; Hirsch, T. K.; Ojamae, L.; Klein, M. L. *Physical Review E (Statistical, Nonlinear, and Soft Matter Physics)* **2006**, *73*, 056113.

(38) Kuo, J.-L.; Coe, J. V.; Singer, S. J.; Band, Y. B.; Ojamae, L. *The Journal of Chemical Physics* **2001**, *114*, 2527.

(39) Kuo, J.-L.; Klein, M. L.; Kuhs, W. F. *The Journal of Chemical Physics* **2005**, *123*, 134505.

(40) Kuo, J.-L. *Physical Chemistry Chemical Physics* **2005**, *7*, 3733.

(41) Kuo, J. L.; Klein, M. L. *J. Phys. Chem. B* **2004**, *108*, 19634.

(42) Kuo, J. L.; Kuhs, W. F. *J. Phys. Chem. B* **2006**, *110*, 3697.

(43) Pauling, L. *Journal of the American Chemical Society* **1935**, *57*, 2680.

(44) Giauque, W. F.; Stout, J. W. *Journal of the American Chemical Society* **1936**, *58*, 1144.

(45) Salzmann, C. G.; Radaelli, P. G.; Slater, B.; Finney, J. L. *Physical Chemistry Chemical Physics*, *13*.

(46) Fukazawa, H.; Ikeda, S.; Mae, S. *Chemical Physics Letters* **1998**, *282*, 215.

(47) Nelmes, R. J.; Loveday, J. S.; Wilson, R. M.; Besson, J. M.; Pruzan, P.; Klotz, S.; Hamel, G.; Hull, S. *Physical Review Letters* **1993**, *71*, 1192.

(48) Abe, K.; Shigenari, T. *The Journal of Chemical Physics*, *134*, 104506.

(49) Salzmann, C. G.; Radaelli, P. G.; Hallbrucker, A.; Mayer, E.; Finney, J. L. *Science* **2006**, *311*, 1758.

(50) Salzmann, C. G.; Radaelli, P. G.; Mayer, E.; Finney, J. L. *Physical Review Letters* **2009**, *103*, 105701.

(51) Tse, J. S.; Ratcliffe, C. I.; Powell, B. M.; Sears, V. F.; Handa, Y. P. *Journal of Physical Chemistry A* **1997**, *101*, 4491.

(52) Blanchard, D.; Riktor, M. D.; Maronsson, J. B.; Jacobsen, H. S.; Kehres, J.; Sveinbjornsson, D.; Bardaji, E. G.; Leon, A.; Juranyi, F.; Wuttke, J.; Hauback, B. C.; Fichtner, M.; Vegge, T. *The Journal of Physical Chemistry C*, *114*, 20249.

(53) Florusse, L. J.; Peters, C. J.; Schoonman, J.; Hester, K. C.; Koh, C. A.; Dec, S. F.; Marsh, K. N.; Sloan, E. D. *Science* **2004**, *306*, 469.

(54) Senadheera, L.; Conradi, M. S. *The Journal of Physical Chemistry B* **2007**, *111*, 12097.

(55) Senadheera, L.; Conradi, M. S. *The Journal of Physical Chemistry B* **2008**, *112*, 13695.

(56) Okuchi, T.; Takigawa, M.; Shu, J. F.; Mao, H. K.; Hemley, R. J.; Yagi, T. *Physical Review B* **2007**, *75*.

(57) Wang, C. Z.; Fasolino, A.; Tosatti, E. *Physical Review B* **1988**, *37*, 2116.

(58) Wang, C. Z.; Chan, C. T.; Ho, K. M. *Physical Review B* **1990**, *42*, 11276.

(59) Lee, C.; Vanderbilt, D.; Laasonen, K.; Car, R.; Parrinello, M. *Physical Review B* **1993**, *47*, 4863.

(60) Goncharov, A. F.; Struzhkin, V. V.; Somayazulu, M. S.; Hemley, R. J.; Mao, H. K. *Science* **1996**, *273*, 218.

(61) Aoki, K.; Yamawaki, H.; Sakashita, M. *Science* **1995**, *268*, 1322.

(62) Reid, C. *Journal of Chemical Physics* **1959**, *30*, 182.

(63) Holzapfe.Wb. *Journal of Chemical Physics* **1972**, *56*, 712.

(64) Lee, C.; Vanderbilt, D.; Laasonen, K.; Car, R.; Parrinello, M. *Physical Review Letters* **1992**, *69*, 462.

(65) Jorgensen, J. D.; Worlton, T. G. *Journal of Chemical Physics* **1985**, *83*, 329.

(66) Benoit, M.; Marx, D. *Chemphyschem* **2005**, *6*, 1738.

(67) Sugimura, E.; Iitaka, T.; Hirose, K.; Kawamura, K.; Sata, N.; Ohishi, Y. *Physical Review B* **2008**, *77*.

Chapter 6

In this chapter, I summarized the achievements during my Ph. D study and presented perspectives for future work. Density function theory (DFT) was employed for all the calculations. From the total enthalpy calculation, we proved that it is successful to locate the ground state structure from the theoretical side in ice XIII. Subsequently, we carried out systematic simulations on oxygen *K* edge X-ray absorption spectroscopy in different ice crystalline phases. And the structural, vibrational properties, and the hydrogen bond symmetrization under compression in hydrogen hydrate (ice-relating material) were addressed with first principle molecular dynamics study.

Conclusions and Future work

6.1 Exploration of hydrogen bond network in ice XIII

Ice XIII is the most complicated ice phase in all experimentally observed phases so far. Experimentalists posed a challenge that it is nontrivial to reproduce their observed structure of ice XIII . Firstly, all the possible hydrogen bond configurations in a unit cell of 28 molecules were successfully generated which follow the ice rule and then we narrowed the calculation scope down to 70 high symmetry structures. We successfully ‘predict’ the most stable structure for different exchange correlation

functionals, LDA and GGA. This also further confirms the validity of DFT in the ice system study.

6.2 Oxygen *K* edge X-ray absorption spectroscopy calculations

Based on the fact that we could locate the most stable structure in different crystalline phases, we moved on to its interesting properties study. It is known that the conventional experimental structural techniques (X-ray diffraction and neutron diffraction pattern) give very similar results even for the very distorted hydrogen bond networks which shows their limited applications to the water system. Recently, there are more and more core-level spectroscopy investigations in elucidating water structure, especially X-ray absorption spectra (XAS). The reason why XAS receives such attentions is that XAS is an effective probe of local environments in an instantaneous way and it is also element specific. Concerning its difficulties in experiments and there still exists controversial issue on the interpretations of the XAS in water, it is essential that we could provide theoretical explanations along with the experimental developments. Ice has a rich phase diagram and its structure is well accepted with near tetrahedral symmetry. Hence, study the XAS in ice system could shed light on the understanding of the controversy mentioned above. Therefore, we carried out systematic and extensive simulations of oxygen *K* edge XAS in different crystalline ice phases. All the factors which may affect the quality of the calculated spectra are examined carefully, like the supercell size, exchange correlation functional, different models (HCH and FCH). Firstly, we arrived at very good agreement in ice I_h

with experimental data and this shows the validity of the model we employed in this thesis and also gives us confidence in the further study in the rest phases of ice.

We found that the pre-edge (~535 eV) is an universal feature appearing in all the ice phases except ice X and the main spectra differences lie in the main peak region (~ 537-540 eV) indicating its great sensitivity to the local hydrogen bond (H-bond) network. Through analyzing the projected electronic density of states, we identified the origin of the oxygen *K* edge XAS spectral features in which transitions of oxygen 1*s*-4a_1 contribute mainly to the pre-edge while the oxygen 1*s*-2b_2 transitions give rise to the main peak feature. The disappearance of pre-edge in ice X can be interpreted as the symmetrization of H-bond which removes the *p* character from 4a_1 level. In addition, we found the delocalization character of 2b_2 orbtials along the H-bond direction which is consistent with the fact that main peak region is more sensitive to the H-bond network. Furthermore, we confirmed that it is reasonable to link the pre-edge feature to the broken H-bond.

6.3 First principles molecular dynamics study in hydrogen hydrate under compression

Based on our study on ice, we moved our target further to the ice-related material, hydrogen hydrate (H_2-H_2O). Research on the hydrogen hydrate has great importance in the astrophysics since H_2 is a major component in the universe and H_2O existence in other planets is already confirmed. Another importance is when consuming

hydrogen hydrate, the only by-product is water, hence, no global warming effects. In the low pressure region, C_2 hydrogen hydrate remains a cubic crystal structure and the structural transitions were observed at approximately 35-40 and 55-60 GPa and the high-pressure phase can survive up to at least 80.3 GPa. However, these two high-pressure phases are not yet determined by the experiments.

We present a study on the structural and vibrational properties of filled ice C_2 hydrogen hydrate under compression by first principles molecular dynamics (FPMD). For the experimentally reported cubic Fd-3m (space group) C_2 phase, this reflects the symmetry at high (room) temperature when the hydrogen bond network is disordered and the hydrogen molecules are orientationally disordered. At low temperature, we found tetragonal symmetry ($P4_12_12$ and $Pna2_1$ space group) in our FPMD. This finding demonstrates that the thermal effects play an essential role in stabilizing the structure to appear as cubic below 40 GPa. We also observed an indication of transition to an unknown high pressure phase above 40 GPa which is consistent with the experimental findings. Moreover, we determined the phase boundary line between hydrogen bond ordered (disordered) phases and the H_2 rotation and non-rotation phases at a rough approximation which may provide hints for further experiments. The vibrational frequencies are extracted from Fourier analysis of the MD trajectories, which are in good agreement with experimental data in the frequency peak positions. Hydrogen bond is predicted to symmetrize below 60 GPa based on the analysis of O-H stretching frequencies and radial distribution function g(OH). In comparison with the pure ice VII, the hydrogen bond symmetrization pressure in C_2 hydrogen hydrate

is much lower as reduced by a factor two.

6.4 Future work

6.4.1 Evaluation of hydrogen bond interaction

The phenomenon of hydrogen bonding attracts wide scientific interest. Weak interactions, including hydrogen bonds, pose challenges to DFT calculations because the conventional exchange correlation functionals, like LDA and GGA, lack the formalism needed to describe properly long-range electron correlation forces.[1,2]

It is well-known that water has a very complex phase diagram. Hence, it would be very meaningful to determine the phase transition pressure, or even map the whole phase diagram theoretically. We calculated the enthalpy of different ice phases (ice I_h I_c, II, III, IV, VI, VII, and XII) as shown in Fig. 6.1. It can be deduced that ice I_h is stable up to 1.83 GPa of 1 order magnitude larger than experimental value of 0.2 GPa. And the second stable phase is ice III from the DFT calculation while it is ice II determined by experiments. Therefore, it is essential to consider the hydrogen bond interaction in the further calculation and reexamine the phase transitions under pressure.

Recently, DFT combined with quantum Monte Carlo has been used the examine the weak interactions (van del Waals force (vdW) and hydrogen bond) in ice.[3] The contribution from vdW lattice energy was found to increase and that from hydrogen bond decrease with pressure. This would influence the relative stabilities between the phases of ice.

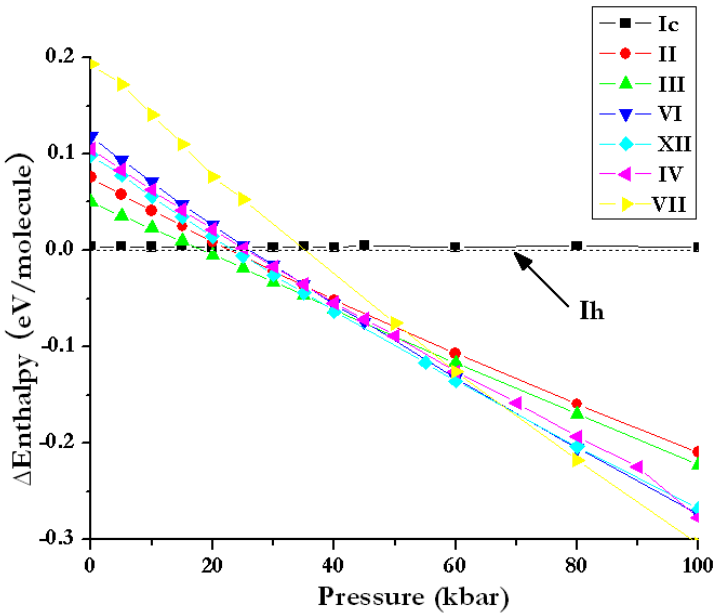

Fig. 6.1 Calculated enthalpy difference (eV/molecule) of ice I_c, II, III, IV, VI, VII, and XII as a function of pressure (kbar) in which the enthalpy of ice I_h was taken as reference.

6.4.2 Study the XAS with Bethe–Salpeter equation

As we all know, DFT is a ground state theory while XAS involves core electron excitation process. However, many modern literatures still use the single-particle theory due to its efficiency. DFT calculations combined with a supercell method gain great success and we adopted this method in this thesis. We mimic the core hole effects by reducing the core hole electron occupation and good agreements with experiment are achieved. Still, Bethe–Salpeter equation (BSE) is a standard and rigorous approach derived from the many body perturbation theory.[4] In order to study 'real' excitation process, we will consider BSE in the next stage. With the aim to include the exciton effects into calculations, we will use the equation of motion for the exciton, the BSE in the next stage.

6.5 References

(1) Kohn, W.; Meir, Y.; Makarov, D. E. *Physical Review Letters* **1998**, *80*, 4153.

(2) Kristyán, S.; Pulay, P. *Chemical Physics Letters* **1994**, *229*, 175.

(3) Santra, B.; Klimes, J.; Alfe, D.; Tkatchenko, A.; Slater, B.; Michaelides, A.; Car, R.; Scheffler, M. *Physical Review Letters*, *107*, 185701.

(4) Onida, G.; Reining, L.; Rubio, A. *Reviews of Modern Physics* **2002**, *74*, 601.